ORIGINAL ARTICLE

Florian Massing · Sebastian Glane · Wolfgang H. Müller ·
Victor A. Eremeyev

Micromorphic theory as a model for blood in the microcirculation: correction and analysis

Abstract This paper analyzes the applicability of Eringen's Generalized Continuum Theories as a model for human blood in the microcirculation. The applied theory considers a fluid with a fully deformable substructure, namely a micromorphic fluid. This analysis is motivated by the fact that blood itself can be considered a suspension of deformable particles, i.e., red blood cells (RBCs), suspended in a Newtonian fluid, i.e., blood plasma. As a consequence, non-Newtonian phenomena such as shear-thinning are observed in blood. To test the micromorphic fluid as a model for blood, the solution for the velocity and the motion of substructure is determined for a cylindrical pipe flow and compared to experimental results of blood flow through narrow glass capillaries representing idealized blood vessels. A similar analysis was also conducted by Kang and Eringen in 1976, but it contains some misprints and minor errors regarding the mathematical expressions and subsequent discussion which are corrected in this paper. For certain material parameters, the micromorphic fluid models capture high-shear blood flow in narrow glass capillaries very well. This concerns both the velocity profiles and the shear-thinning behavior. Furthermore, a parameter study reveals that the flexibility of substructure governs the micromorphic shear-thinning. In this regard, parallels can be drawn to the shear-thinning of human blood, which is also induced by the deformability of RBCs. This makes the micromorphic fluid a complex but accurate model for human blood, at least for the considered experiments.

1 Introduction

Cardiovascular diseases (CVDs) as leading cause of death worldwide, accounting for about "32% of all global deaths" in 2019, [38], are highly relevant in many fields of study, such as drug development or medical engineering. To reduce the morbidity due to CVDs, several prevention measures can be taken, including drugs and surgery next to behavioral measures. For the development of such measures, a comprehensive knowledge of the physical and chemical properties of blood is required. However, because blood is not a simple fluid such as water, its physical properties are in general not explained by the well-known equations of motion for a simple fluid either. Therefore, this paper starts from a generalized continuum approach as a model for

Communicated by Andreas Öchsner.

F. Massing (✉) · S. Glane · W. H. Müller
Institute of Mechanics, Chair of Continuum Mechanics and Constitutive Theory, Technische Universität Berlin, Sekr. MS. 2, Einsteinufer 5, 10587 Berlin, Germany
E-mail: f.massing@tu-berlin.de

V. A. Eremeyev
Department of Civil and Environmental Engineering and Architecture (DICAAR), University of Cagliari, Via Marengo, 2, 09123 Cagliari, Italy

blood in narrow blood vessels, developed by Eringen in 1964. For a better understanding of the considered approach and the related experiments, a brief introduction to the two fields relevant for this paper, namely hemodynamics and Eringen's micro-continuum theories, is given below. Then, the governing equations of a micromorphic fluid are stated. They are subsequently used to determine the motion and the micromotion of a micromorphic fluid in a cylindrical tube. After validating the derived results, the motion of the micromorphic fluid is compared to human blood flowing through narrow glass capillaries in Sect. 4. This problem was already solved and discussed by Kang and Eringen in 1976, leading to promising conclusions [22]. However, their solution contains some misprints and the derivation of their results was not documented, so the results are not reproducible. The purpose of this paper is to evaluate, whether the conclusions made in [22] are still valid.

1.1 Hemodynamics

Human blood can be construed as a tissue, an emulsion or a two-phase fluid, depending on the field of study. However, in the rheological context of this paper, it is considered as a fluid in which particles are suspended. Most importantly, it can, in general, not be considered as a Newtonian fluid. This is because it has many properties that are not covered by classic fluid mechanics. The aim of this section is to point out the differences to a Newtonian fluid by listing and—as far as possible—explaining several phenomena leading to these differences. To be able to do so, it is useful to understand, what exactly blood is, and thus, what components it is composed of.

Human blood and that of vertebrates, in general, consists of an aqueous solution, namely plasma, and different particles, i.e., RBCs, white blood cells (WBCs) and platelets. Of these, the RBCs have the highest volume fraction, or Hematocrit (Ht), of about 40% to 45% [33]. The blood plasma makes up the highest volume fraction of blood and can be considered a Newtonian fluid. It consists mainly of water, but also contains "organic molecules, proteins, and salts," [3, p. 435]. The plasma viscosity at 37 °C usually takes values of 1.1 mPa s to 1.3 mPa s [23], whereas the viscosity of whole blood cannot be described by a single value, because it varies with changing flow situations, as discussed below. As a consequence of the high hematocrit, this behavior is primarily attributed to the RBCs [26]. Under special circumstances, WBCs and platelets can also have a severe impact on the motion of blood, for example through platelet adhesion and aggregation due to injured blood vessel and high shear rates leading to thrombosis, as explained in [28]. But these special circumstances are not considered in this work.

As mentioned above, the hematocrit has a major influence on blood flow properties: For example, an increased hematocrit yields an increased viscosity for all vessel sizes and shear rates [20]. The larger viscosity due to more cells suspended in plasma is a logical consequence of rigid particles disturbing the streamlines and thereby increasing the flow resistance [5]. At a sufficiently large shear rate, a migration of RBCs toward the center of the vessel is observed, resulting in a high local hematocrit in the inner vessel and a RBC-free plasmatic zone near the vascular wall. Consequently, the local viscosity near the vessel wall corresponds to that of plasma, whose value is close to that of water and many times smaller than that of blood in large vessels. As a result, the blood flows without any particle-wall-interaction-induced flow resistance through the vessel, which promotes a decreased viscosity for whole blood. While the formation of a plasmatic layer occurs for every vascular radius, experiments indicate that the absolute thickness of this layer does not change along the vessel radius but is fixed at about 1.8 μm [31,32]. Hence, the reduced viscosity for larger radii is negligible. This effect is generally referred to as shear-thinning or, in the context of blood Fåhræus–Lindqvist effect, see [13]. Shear-thinning is characterized by the apparent viscosity, which is derived from the Hagen–Poiseuille equation [25,33]:

$$\mu_{\text{app}} = \frac{\pi}{8} \frac{\Delta p}{L} \frac{R^4}{Q}. \tag{1.1}$$

Here, $\Delta p/L$, R and Q denote the pressure drop along the distance L, the vessel radius and the volume flow rate, respectively. For sufficiently large shear rates, the volume flow rate Q is approximately proportional to the pressure drop $\Delta p/L$ multiplied by a factor $M(R)$, which only depends on the vessel radius R. Hence, the asymptotic apparent viscosity is defined as a function of R [19,21]:

$$\mu_{\text{app}}(R) := \lim_{Q \to \infty} \frac{\pi}{8} \frac{\Delta p}{L} \frac{R^4}{Q} \quad \Rightarrow \quad \mu_{\text{app}}(R) = \frac{\pi}{8} \frac{R^4}{M(R)}. \tag{1.2}$$

The error of this approximation was found to be negligible for pseudo-shear rates $\overline{v} > 50 s^{-1}$ which is a measure for the actually occurring shear rates [29]:

$$\overline{v} := \frac{v_{\mathrm{m}}}{2R}, \qquad v_{\mathrm{m}} := \frac{Q}{\pi R^2}, \tag{1.3}$$

Here, v_{m} denotes the volumetrically averaged velocity.

It has been shown that for $R < 300\,\mu\mathrm{m}$ the apparent viscosity decreases significantly, monotonously with a decreasing vessel radius [13]. Consequently, in smaller vessels blood becomes continuously less viscous. Since most of RBCs are packed near the vessel center, they flow with similar velocity as the surrounding particles, forming a plug-shaped velocity profile, cf., [15]. It can be proven that the cell-free layer formation and the Fåhræus–Lindqvist effect are a result of RBC deformability inducing axial migration, whereas the exact mechanisms leading to fluidity in the core region are not clear yet [16]. While recent studies indicate that a simple deformation of RBCs along the streamlines might be the cause of shear-thinning in the vessel core region [24], another possible explanation is an extraordinary deformation called tank-treading that provokes a drop-like behavior [37]. The RBC deformation in the core region further reduces the viscosity of blood.

A direct consequence of the cell-free layer is the so-called Fåhræus effect, which was discovered in 1929: The majority of RBCs in the cross section of a narrow blood vessel are located near the vessel core. Obviously, the average of the velocity in this RBC-rich core is significantly higher than the average plasma velocity along the vessel cross section, especially because a larger fraction of plasma is located near the vessel walls as compared to a homogeneous solution. Thus, in average in a narrow vessel RBCs travel faster than the suspending plasma. Consequently, the average volume fraction of RBCs in a cross section, namely the true Hematocrit, must be smaller than the Hematocrit of the whole blood [12]. This variable relation between true tube Hematocrit and feed Hematocrit is referred to as the Fåhræus effect and was shown to decrease with decreasing vessel radius and with decreasing feed hematocrit [2].

1.2 Micro-continuum approach

In this study, the micromorphic theory is used as a continuum model for blood. This theory was introduced by Eringen and Suhubi for solid materials and adjusted by Eringen to model fluent media [6,8]. The approach aims at describing media with a deformable substructure by considering the actual rotation and deformation of substructure on a continuum level. Note that there are other continuum mechanical approaches applied to non-Newtonian fluid problems, where the non-Newtonian behavior is modeled by identifying mathematical instead of phenomenological relations governing the material behavior. For instance, the gradient theory from [34] considers a stress tensor containing higher gradients of the strain-rate, whereas the stress tensor in the micromorphic approach contains the micromotion instead, as shown below.

For a micromorphic material, each material point is considered the center of mass of a deformable particle of infinitesimal size. The position of a material point is described by the vector X or x in the reference or current configuration, respectively. Analogously, on the micro-level, the infinitesimal vectors Ξ and ξ describe the position of a material point within a particle with respect to its center of mass in the reference and current configuration, respectively. The inverse motion and inverse micromotion are required to exist and to be unique, because two material points cannot be located at the same spatial point simultaneously. In order to relate differential line elements in the two configurations, the deformation tensor F and the micromotion tensor χ are introduced [8]:

$$F(X, t) = \frac{\partial x_k}{\partial X_M} e_k \otimes E_M, \qquad \chi(X, t) = \frac{\partial \xi_k}{\partial \Xi_M} e_k \otimes E_M. \tag{1.4}$$

As indicated by the lower and upper case index letters, F and χ depend on both the current and reference configuration and are two-point tensors. Similar to the macro-scale deformation tensor, the micromotion tensor describes the particle deformation on the micro-scale. Thereby, it approximately links the microscopic position vectors in the two configurations via [8]:

$$\xi = \chi \cdot \Xi. \tag{1.5}$$

Furthermore, the determinants of both F and χ are assumed to be positive, in order to 'retain the right-hand screw orientations of the frames-of-references,' [10, p. 6]. This is sufficient for the inverse tensors F^{-1} and

χ^{-1} to exist. The Eulerian velocity gradient $\boldsymbol{L}$ and gyration tensor $\boldsymbol{G}$ are defined as [8]:

$$\boldsymbol{L} = \boldsymbol{v} \otimes \nabla = \dot{\boldsymbol{F}} \cdot \boldsymbol{F}^{-1}, \qquad \boldsymbol{G} = \dot{\boldsymbol{\chi}} \cdot \boldsymbol{\chi}^{-1}, \tag{1.6}$$

where $\boldsymbol{v}$ is the velocity field, ∇ denotes the del or nabla operator, and a superscript dot indicates the Lagrangian or material derivative:

$$\dot{\boldsymbol{\phi}} := \frac{\mathrm{d}\boldsymbol{\phi}}{\mathrm{d}t} = \frac{\partial \boldsymbol{\phi}}{\partial t} + (\boldsymbol{\phi} \otimes \nabla) \cdot \mathbf{v}. \tag{1.7}$$

The micromotion induces a particle deformation on the micro-scale which is accompanied by a change of the mass distribution, characterized by the microinertia tensor $\boldsymbol{i}$ [8]:

$$\varrho \boldsymbol{i} \, \mathrm{d}v = \int_{\mathrm{d}v} \varrho' \boldsymbol{\xi} \otimes \boldsymbol{\xi} \, \mathrm{d}v'. \tag{1.8}$$

Here, ϱ and $\mathrm{d}v$ denote the density and an infinitesimal volume element in the current configuration, respectively, while the superposed prime indicates the corresponding quantity on the micro-scale. Definition (1.8) slightly deviates from the definition of the inertia tensor commonly used in classical mechanics [17]. However, the two formulations can be transformed into each other, as described in [36]. By the use of the inertia tensor $\boldsymbol{i}$ and gyration tensor $\boldsymbol{G}$, the spin inertia per unit mass $\boldsymbol{\sigma}$ [6] is defined:

$$\boldsymbol{\sigma} = \left(\frac{\mathrm{d}\boldsymbol{G}}{\mathrm{d}t} + \boldsymbol{G} \cdot \boldsymbol{G} \right) \cdot \boldsymbol{i}. \tag{1.9}$$

The spin inertia itself is not a time-rate, though it contains the material derivative of the gyration tensor. It characterizes the change in time of a particle's spin angular momentum (cf. [36]). The field quantities introduced in this section are used to formulate the governing balance and constitutive equations of a micromorphic fluid below.

2 Micromorphic fluid theory

This section comprises the governing equations to describe the motion of a micromorphic fluid in the current configuration. Apart from fields of velocity, temperature, and pressure known from classical fluid mechanics, micromorphic theory additionally depends on the gyration tensor $\boldsymbol{G}$ which consists of nine independent components as introduced above. For a better interpretation, this tensor can be decomposed into its symmetric part $\mathrm{sym}(\boldsymbol{G})$ representing the microshearing and stretching, and its skew-symmetric part $\mathrm{skw}(\boldsymbol{G})$ representing the microrotation. The evolution of these fields is also explained by the balance equations stated below.

2.1 Balance equations

The balance equations are presented in their local form since they are required to hold in every arbitrary infinitesimal control volume $\mathrm{d}v$ within the domain Ω. On the boundary $\partial \Omega$, certain jump conditions resulting from boundary integrals in the balances' global form must hold, if no Dirichlet boundary conditions are specified. These will not be stated in this article, but further information on them can be found in [6]. In addition, all balance equations stated in this subsection can also be found in [6]. First, the usual local form of the balance of mass is given by

$$\frac{\mathrm{d}\varrho}{\mathrm{d}t} + \varrho (\mathbf{v} \cdot \nabla) = 0. \tag{2.1}$$

The momentum equation reads

$$\nabla \cdot \mathbf{t} + \varrho \left(\mathbf{f} - \frac{\mathrm{d}\mathbf{v}}{\mathrm{d}t} \right) = \mathbf{0}. \tag{2.2}$$

Here, $\mathbf{f}$ and $\mathbf{t}$ are the external body force and stress tensor, respectively. In contrary to classical continuum mechanics, the stress tensor is usually not symmetric for microfluids. The micro-motion is governed by the so-called micro-spin balance,

$$\nabla \cdot \overset{(3)}{\boldsymbol{\lambda}} + \mathbf{t} - \mathbf{s} + \varrho\,(\mathbf{l} - \boldsymbol{\sigma}) = \mathbf{0}, \tag{2.3}$$

and depends on the symmetric micro-stress average tensor $\mathbf{s}$, the first moments stress tensor of third-order $\overset{(3)}{\boldsymbol{\lambda}}$, and the external moments tensor $\mathbf{l}$. Here, the micro-stress average tensor corresponds to the averaged stress tensor of a point particle. It can be obtained from the momentum equation within a particle, see [8]. The balance of angular momentum of a point particle is fulfilled, if the corresponding micro-stress is symmetric, because a point particle itself does not contain a microstructure. Since the spin inertia $\boldsymbol{\sigma}$ contains the material derivative of $\boldsymbol{G}$, Eq. (2.3) corresponds to a balance equation describing the micromotion's change in time. The microinertia is assumed to be conserved, which is formalized by the following identity:

$$\varrho\frac{\mathrm{d}\epsilon}{\mathrm{d}t} = \mathbf{t} \cdot\!\cdot (\nabla \otimes \mathbf{v}) + (\mathbf{s} - \mathbf{t}) \cdot\!\cdot \mathbf{G}^{\mathsf{T}} + \overset{(3)}{\boldsymbol{\lambda}} \cdot\!\cdot\!\cdot (\nabla \otimes \mathbf{G}) + \nabla \cdot \mathbf{q} + \varrho h, \tag{2.4}$$

Furthermore, the balance of internal energy is given by

$$\varrho\frac{\mathrm{d}\epsilon}{\mathrm{d}t} = \mathbf{t} \cdots (\nabla \otimes \mathbf{v}) + (\mathbf{s} - \mathbf{t}) \cdots \mathbf{G}^{\mathsf{T}} + \overset{(3)}{\boldsymbol{\lambda}} \cdots (\nabla \otimes \mathbf{G}) + \nabla \cdot \mathbf{q} + \varrho h, \tag{2.5}$$

where ε, $\mathbf{q}$ and h denote the specific internal energy density, the heat vector field, and a heat source, respectively. Moreover, the double dot operator "$\cdot\!\cdot$" is defined through

$$A_{ij}\mathbf{e}_i \otimes \mathbf{e}_j \cdot\!\cdot B_{kl}\mathbf{e}_k \otimes \mathbf{e}_l = A_{ij}B_{ij}. \tag{2.6}$$

Finally, the Clausius–Duhem inequality in differential representation

$$-\varrho\left(\frac{\mathrm{d}\psi}{\mathrm{d}t} + \eta\frac{\mathrm{d}\theta}{\mathrm{d}t}\right) + \mathbf{t} \cdot\!\cdot (\nabla \otimes \mathbf{v}) + (\mathbf{s} - \mathbf{t}) \cdot\!\cdot \mathbf{G} + \overset{(3)}{\boldsymbol{\lambda}} \cdots (\mathbf{G} \otimes \nabla)^{\mathsf{T}} + \frac{1}{\theta}\mathbf{q} \cdot (\theta\nabla) \geq 0 \tag{2.7}$$

assures that the second law of thermodynamics is not violated [10]. Here, η and θ denote the specific entropy and the absolute temperature, respectively, while $\psi = \epsilon - \theta\eta$ represents the Helmholtz free energy. Since in this article only non-heat-conducting materials are considered, the energy balance will not be solved.

2.2 Constitutive equations

In order to obtain a set of Partial Differential Equations (PDEs) governing the microfluid fields, constitutive equations need to be employed. In this article, the linear constitutive equations from [6] are used if not stated otherwise. First, the non-symmetric stress tensor

$$\mathbf{t} = (-\pi + \lambda_v\mathbf{v} \cdot \nabla + \lambda_0\mathbf{1} \cdot\!\cdot \mathbf{G})\mathbf{1} + 2\mu_v\mathbf{d} + 2\mu_0(\mathbf{G} - \mathbf{w}) + 2\mu_1(\mathbf{G}^{\mathsf{T}} + \mathbf{w}) \tag{2.8}$$

links the stress to the velocity gradient, the gyration tensor, and the thermodynamic pressure π, and contains the viscosity coefficients λ_v, λ_0, μ_v, μ_0, and μ_1 as material parameters. Moreover, the velocity gradient was decomposed into its symmetric part, i.e., the strain-rate tensor $\boldsymbol{d} = \mathrm{sym}(\boldsymbol{v} \otimes \nabla)$, and its skew-symmetric part, namely the vorticity tensor $\boldsymbol{w} = \mathrm{skw}(\boldsymbol{v} \otimes \nabla)$. The average micro-stress tensor

$$\mathbf{s} = (-\pi + \eta_v\mathbf{v} \cdot \nabla + \eta_0\mathbf{1} \cdot\!\cdot \mathbf{G})\mathbf{1} + 2\mu_v\mathbf{d} + 2\zeta_2\mathrm{sym}\mathbf{G} \tag{2.9}$$

depends on the velocity gradient and on the gyration tensor as well as on the material parameters η_v, η_0 and ζ_2. By equating these parameters with the corresponding ones in the stress tensor, i.e., $\eta_v = \lambda_v$ and $\eta_0 = \lambda_0$,
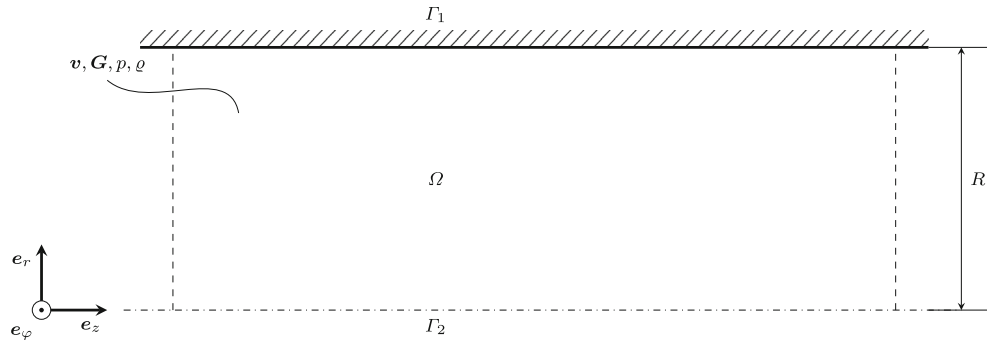
Fig. 1 Underlying domain

the governing equations reduce to the Navier–Stokes equations in the absence of micromotion, i.e., if $\boldsymbol{G} = \boldsymbol{w}$ [6]. Finally, the first stress moments tensor

$$
\begin{aligned}
\overset{(3)}{\boldsymbol{\lambda}} &= \mathbf{1} \otimes (\gamma_1 \mathbf{G} \cdot \nabla + \gamma_2 \nabla \cdot \mathbf{G} + \gamma_3 (\mathbf{1} \cdot\cdot \mathbf{G}) \nabla) \\
&\quad + \mathbf{1} \otimes (\gamma_4 \mathbf{G} \cdot \nabla + \gamma_5 \nabla \cdot \mathbf{G} + \gamma_6 (\mathbf{1} \cdot\cdot \mathbf{G}) \nabla) \cdot\cdot \overset{(4)}{\mathsf{T}} \\
&\quad + (\gamma_7 \mathbf{G} \cdot \nabla + \gamma_8 \nabla \cdot \mathbf{G} + \gamma_9 (\mathbf{1} \cdot\cdot \mathbf{G}) \nabla) \otimes \mathbf{g} \\
&\quad + \gamma_{10} \mathbf{G} \otimes \nabla + \gamma_{11} (\mathbf{G} \otimes \nabla) \cdot\cdot \overset{(4)}{\mathsf{T}} + \gamma_{12} \mathbf{G}^\mathsf{T} \otimes \nabla \\
&\quad + \gamma_{13} (\mathbf{G}^\mathsf{T} \otimes \nabla)^\mathsf{T} + \gamma_{14} \nabla \otimes \mathbf{G} + \gamma_{15} \nabla \otimes \mathbf{G}^\mathsf{T}
\end{aligned}
\tag{2.10}
$$

introduces 15 new gyration viscosity coefficients γ_i and, furthermore, depends on the gyration tensor, the metric tensor $\mathbf{g}$, and the transposition tensor $\overset{(4)}{\mathsf{T}} := \mathbf{e}_i \otimes \mathbf{e}_j \otimes \mathbf{e}_j \otimes \mathbf{e}_i$. The first stress moments tensor represents the "surface tractions acting on the [particle] surfaces," [8, p. 194] and thereby affects the stress on the macro-scale via Eq. (2.3). It should be mentioned that in more recent works, a different representation of the constitutive equations is chosen. For example in [11], the first moments stress tensor only depends on 11 viscosity coefficients but is also independent of the metric tensor. Usually, the viscosity coefficients are functions of the temperature, but due to the neglect of non-heat-conductive media, they can be treated as material constants.

3 Blood as a micromorphic in idealized narrow blood vessels

In this section, blood flow in a cylindrical pipe, which can be regarded as an idealized blood vessel is modeled as a micromorphic fluid. In order to assess how suitable the micromorphic model is, the hemodynamic properties of a micromorphic fluid are analyzed. This is achieved by deriving the solution to the laminar flow problem. Precisely, the solution of the Boundary Value Problem (BVP) is found for the laminar incompressible stationary case. Such a solution is not only valuable to determine restrictions on material parameters for blood but also serves as a reference solution for the validation of numerical solutions. A solution of the problem was already presented in [22], but it contains minor errors which also affect the final results. Therefore, the correct solution is presented and also validated in the following.

3.1 Assumptions and boundary conditions

The domain corresponds to a circular pipe with radius R, and the problem will therefore be solved in cylindrical coordinates. Thus, the domain can be expressed as

$$
\Omega := \left\{ [r, \varphi, z] \in \mathbb{R}^3 \,|\, 0 \le r < R, \ 0 \le \varphi < 2\pi \right\}.
$$

A sketch of this domain is shown in Fig. 1. Furthermore, the assumption of rotational symmetry allows to solve the problem in the r-z-plane:

$$\Omega := \left\{ [r, z] \in \mathbb{R}^2 \mid 0 < r < R \right\}.$$

Accordingly, the former physical boundary at the pipe wall $\Gamma_1 := \{[r, z] \in \mathbb{R}^2 \mid r = R\}$ and the cylinder axis $\Gamma_2 := \{[r, z] \in \mathbb{R}^2 \mid r = 0\}$ are defined, and make up the boundary of the computational domain:

$$\partial\Omega = \Gamma_1 \cup \Gamma_2, \quad \overline{\Omega} = \Omega \cup \partial\Omega.$$

Another consequence of rotational symmetry is that the microrotation tensor contains only two components spanned by $\mathbf{e}_r$ and $\mathbf{e}_z$, and therefore, the micro-rotation reads

$$\text{skw}(\mathbf{G}) = \frac{G_{rz} - G_{zr}}{2} \left[\mathbf{e}_r \otimes \mathbf{e}_z - \mathbf{e}_z \otimes \mathbf{e}_r \right]. \tag{3.1}$$

Analogously, the micro-shearing only occurs due to motion in the r-z-plane. This means

$$\text{sym}(\mathbf{G}) = \frac{G_{rz} + G_{zr}}{2} \left[\mathbf{e}_r \otimes \mathbf{e}_z + \mathbf{e}_z \otimes \mathbf{e}_r \right], \tag{3.2}$$

where the migration velocities G_{rr} and G_{zz} were neglected, because they are usually small in crowded suspensions [22]. In addition, the fluid is assumed to flow parallel to the vessel wall, while the fields $\boldsymbol{v}$ and $\boldsymbol{G}$ only change along r:

$$\boldsymbol{v} = v(r)\boldsymbol{e}_z, \tag{3.3a}$$
$$\boldsymbol{G} = G_{rz}(r)\boldsymbol{e}_r \otimes \boldsymbol{e}_z + G_{zr}(r)\boldsymbol{e}_z \otimes \boldsymbol{e}_r. \tag{3.3b}$$

Therefore, the microinertia $\boldsymbol{i}$ is also a function of r. Because of the assumption of incompressibility, the conservation of mass (Eq. (2.1)) reduces to the incompressibility condition:

$$\boldsymbol{v} \cdot \nabla = 0.$$

Accordingly, the micro-incompressibility is assumed:

$$\mathbf{G} \cdot\cdot \mathbf{1} = 0.$$

Furthermore, the flow is assumed to be stationary, such that all partial derivatives with respect to time vanish. As a consequence of the assumptions, the convective term also vanishes:

$$\frac{\partial\boldsymbol{\phi}}{\partial t} = \mathbf{0}, \quad (\boldsymbol{\phi} \otimes \nabla) \cdot \boldsymbol{v} = \mathbf{0} \quad \Rightarrow \quad \frac{d\boldsymbol{\phi}}{dt} = \mathbf{0}. \tag{3.4}$$

Finally, external body forces or moments of any kind are not considered. The constitutive equations (2.2) can be substituted in the balance equations (2.1), which allows to simplify the BVP, as derived in the following.

3.2 Boundary conditions

The boundary condition for the velocity field corresponds to the typical homogeneous Dirichlet or no-slip boundary condition on Γ_1:

$$\boldsymbol{v}(R) = \mathbf{0}.$$

For the gyration tensor, on the other hand, the postulation of boundary conditions is not that simple: Multiple different boundary conditions, such as (in-)homogeneous Dirichlet boundary conditions, see [7], or homogeneous Neumann boundary conditions for the micro-rotation are possible, see also [1,22]. However, here a coupling boundary condition is applied. This is motivated by the fact that the velocity gradient is the only field having a direct effect on the suspended particles. The vorticity will cause the particles to rotate near the wall,

while the shearing of the fluid will induce a shearing and stretching of the particles. Formally, this effect is expressed as [22]

$$\mathbf{G}(r = R) = \left(\lambda_1(\boldsymbol{v} \cdot \nabla)\mathbf{1} + \lambda_2\boldsymbol{d} + \lambda_3\boldsymbol{w}\right)\Big|_{r=R}. \tag{3.5}$$

The coupling parameters λ_2 and λ_3 can be obtained from a comparison with the linear and angular velocity of a rigid, spherical particle in a dilute suspension, respectively: This particle is assumed to roll and slip along the wall, depending on the concentration of the suspension, i.e., the hematocrit. The linear and angular velocity were derived using perturbation methods in [22]. For a crowded suspension of deformable particles, these findings are applied by relating the microshearing and microstretching to the derived linear particle velocity and adjusting the derived particle rotation by a crowding factor $(1 - \mathrm{Ht})$ to account for frictional effects [22]:

$$\lambda_2 = 1 - \frac{5}{16}\mathrm{Ht}, \qquad \lambda_3 = \left(1 - \frac{5}{16}\mathrm{Ht}\right)(1 - \mathrm{Ht}). \tag{3.6}$$

The remaining coupling parameter λ_1 is irrelevant in this case due to the incompressibility condition, but it is linked to the migration velocity and assumed to vanish anyway [22].

Finally, all fields are required to be regular on $\overline{\Omega}$, which will result in mathematical boundary conditions on Γ_2, as shown during the derivation of the solution.

3.3 Constitutive equations and viscosity coefficients

Under the assumptions stated in Sect. 3.1, the constitutive equations simplify to [22]:

$$\mathbf{t} = -\pi\mathbf{1} + 2\mu\boldsymbol{d} + \zeta_1\mathrm{sym}(\mathbf{G}) + \kappa[\mathrm{skw}(\mathbf{G}) - \boldsymbol{w}], \tag{3.7a}$$

$$\mathbf{s} = -\pi\mathbf{1} + 2\mu\boldsymbol{d} + 2\zeta_2\mathrm{sym}(\mathbf{G}), \tag{3.7b}$$

$$\begin{aligned} \overset{\langle 3 \rangle}{\boldsymbol{\lambda}} &= \mathbf{1} \otimes (\gamma_1\mathbf{G} \cdot \nabla + \gamma_2\nabla \cdot \mathbf{G}) + \mathbf{1} \otimes (\gamma_4\mathbf{G} \cdot \nabla + \gamma_5\nabla \cdot \mathbf{G}) \overset{\langle 4 \rangle}{\cdot\cdot \mathsf{T}} \\ &+ (\gamma_7\mathbf{G} \cdot \nabla + \gamma_8\nabla \cdot \mathbf{G}) \otimes \mathbf{g} + \gamma_{10}\mathbf{G} \otimes \nabla + \gamma_{11}(\mathbf{G} \otimes \nabla) \overset{\langle 4 \rangle}{\cdot\cdot \mathsf{T}} \\ &+ \gamma_{12}\mathbf{G}^\mathsf{T} \otimes \nabla + \gamma_{13}(\mathbf{G}^\mathsf{T} \otimes \nabla)^\mathsf{T} + \gamma_{14}\nabla \otimes \mathbf{G} + \gamma_{15}\nabla \otimes \mathbf{G}^\mathsf{T}, \end{aligned} \tag{3.7c}$$

where the new viscosity coefficients μ, ζ_1, ζ_2 consist of combinations of viscosity coefficients introduced in Sect. 2.2, which are given by [22]

$$\mu := \mu_v + \kappa/2 \qquad \zeta_1 := 2(\mu_0 + \mu_1), \qquad \kappa = 2(\mu_0 - \mu_1). \tag{3.8}$$

Substituting Eqs. (3.7) in the Clausius–Duhem inequality (2.7) yields multiple restrictions on the viscosity coefficients, of which the most important ones are given by [22, p. 145]:

$$\mu \geq 0, \qquad 2\zeta_2 - \zeta_1 \geq \kappa \geq 0, \qquad 4\mu(\zeta_2 - \zeta_1/2) - (\zeta_1/2)^2 \geq 0,$$

$$\sum_{i=0}^{15} \gamma_i \geq 0, \qquad \gamma_2 + \gamma_{11} + \gamma_{14} \geq 0, \qquad \gamma_{14} \geq 0, \qquad \gamma_{14} \geq \gamma_{15}, \tag{3.9}$$

$$\gamma_{14} \geq \gamma_{10} + \gamma_{13}, \qquad \gamma_{14} \geq \gamma_{12}, \qquad \cdots$$

Furthermore, in the context of blood, several conclusions regarding the magnitudes of the viscosity coefficients and trends with respect to the initial hematocrit were made in [22]. They originate from a comparison with the stress tensor for dilute suspensions [14]. Since blood is not considered a dilute but a dense suspension, they cannot be adopted one-to-one. The findings do not include how crowded particles affect each other, but the remaining findings are still assumed to hold:

– μ increases with increasing hematocrit.

- $|\zeta_1|$ and $|\zeta_2|$ also increase with increasing hematocrit, but at a higher rate than μ, because they govern the influence of deformability on the resulting stress. Hence, larger concentration yields stronger interactions between particles. This effect will, for a dense suspension, exceed the effect of particles influencing each other via the surrounding fluid.
- κ, on the other hand, represents the stress due to particle rotation, and thus will also increase at a higher rate than μ. It is of the same order of magnitude as ζ_2, but cannot have a larger order of magnitude than μ.
- The rotational viscosity coefficients γ_i correspond, if normalized by μ, to a characteristic length of the particles and are therefore chosen such that $\sqrt{\gamma_i/\mu}$ matches the size of particles, i.e., around e-6m to e-5m.

3.4 Solution to the micromorphic pipe flow

The steady flow of a micromorphic fluid as described above is summarized by the following BVP in tensor representation:

$$
\text{BVP} = \begin{cases}
\nabla \cdot \mathbf{t} & = \mathbf{0}, & 0 \leq r < R, \\
\nabla \cdot \overset{(3)}{\boldsymbol{\lambda}} + \mathbf{t} - \mathbf{s} & = \mathbf{0}, & 0 \leq r < R, \\
\mathbf{v} & = \mathbf{0}, & r = R, \\
\mathbf{G} - (\lambda_2 \mathbf{d} + \lambda_3 \mathbf{w}) & = \mathbf{0}, & r = R.
\end{cases} \tag{3.10}
$$

The final solutions to this BVP are stated here, while a comprehensive derivation is given in "Appendix A." The solutions are stated as functions of the normalized radial coordinate $\rho := r/R$, while the solutions themselves are normalized by

$$
v_0 := -\frac{PR^2}{4\mu}, \qquad \text{where} \quad P := \frac{\mathrm{d}p}{\mathrm{d}z}.
$$

The expression for the velocity field reads

$$
\begin{aligned}
\frac{v(\rho)}{v_0} = 1 - \rho^2 + \frac{1}{\mu + \kappa/2} \Bigg[& \frac{C_{1\star}(I_0(L) - I_0(L\rho))}{2L} \Big(\zeta_1(1 + f_1) + \kappa(1 - f_1) \Big) \\
& + \frac{C_{2\star}(I_0(M) - I_0(M\rho))}{2M} \Big(\zeta_1(1 + f_2) + \kappa(1 - f_2) \Big) \Bigg],
\end{aligned} \tag{3.11}
$$

and the micromotion is given by

$$
\frac{R}{v_0} G_{(rz)}(\rho) = \frac{C_{1\star}}{2}(1 + f_1)I_1(L\rho) + \frac{C_{2\star}}{2}(1 + f_2)I_1(M\rho), \tag{3.12a}
$$

$$
\frac{R}{v_0} G_{[rz]}(\rho) = \rho + \frac{C_{1\star}}{2}(1 - f_1)I_1(L\rho) + \frac{C_{2\star}}{2}(1 - f_2)I_1(M\rho), \tag{3.12b}
$$

where $G_{(ij)}$ and $G_{[ij]}$ denote the components of $\mathrm{sym}(\mathbf{G})$ and $\mathrm{skw}(\mathbf{G})$, respectively. The constants $C_{1\star}$ and $C_{2\star}$ within the solutions are:

$$
\begin{aligned}
C_{1\star} &= \frac{(f_2 - 1)\mu/a\lambda_2 - (1 + f_2)\mu/a\lambda_3 + (1 + f_2)}{I_1(L)(f_1 - f_2)}, \\
C_{2\star} &= \frac{(1 - f_1)\mu/a\lambda_2 + (1 + f_1)\lambda_3\mu/a - (1 + f_1)}{I_1(M)(f_1 - f_2)}, \\
a &= \mu + \frac{\kappa}{2} + \frac{\lambda_2 \zeta_1}{2} - \frac{\lambda_3 \kappa}{2}, \qquad L = \alpha R, \qquad M = \beta R, \\
f_1 &= -\frac{(\alpha^2 - \alpha_2^2)}{(\alpha^2 - \alpha_1^2)}\frac{K_2}{K_1}, \qquad f_2 = -\frac{(\beta^2 - \alpha_2^2)}{(\beta^2 - \alpha_1^2)}\frac{K_2}{K_1}.
\end{aligned}
$$

Here, α and β are the positive solutions of the following equation:

$$
(\lambda^2 - \alpha_1^2)(\lambda^2 - \alpha_4^2)K_1 K_4 - (\lambda^2 - \alpha_2^2)(\lambda^2 - \alpha_3^2)K_2 K_3 \overset{!}{=} 0.
$$

The α_i^2 and K_i are composed of viscosity coefficients as follows:

$$K_1 = \gamma_1 + \gamma_{13} + \gamma_{15} + \gamma_4 + \gamma_{12} + \gamma_{14}, \qquad K_2 = \gamma_2 + \gamma_{11} + \gamma_{14} + \gamma_5 + \gamma_{10} + \gamma_{15},$$
$$K_3 = \gamma_1 + \gamma_{13} + \gamma_{15} - (\gamma_4 + \gamma_{12} + \gamma_{14}), \qquad K_4 = \gamma_2 + \gamma_{11} + \gamma_{14} - (\gamma_5 + \gamma_{10} + \gamma_{15}),$$
$$\alpha_1^2 = -(\zeta_1 - 2\zeta_2)/K_1, \qquad \alpha_2^2 = -(\zeta_1 - 2\zeta_2)/K_2,$$
$$\alpha_3^2 = -\kappa(2\mu + \zeta_1)/(K_3(2\mu + \kappa)), \qquad \alpha_4^2 = \kappa(2\mu - \zeta_1)/(K_4(2\mu + \kappa)).$$

In the following, the obtained solutions are presented and discussed for some special cases. Here, Eqs. (3.12) and (3.11) correspond to Eqs. (5.8) from [22, p. 149], although, the constants $C_{1\star}$ and $C_{2\star}$ deviate from these used in [22], which will also be investigated below.

4 Results and discussion

By means of the solution obtained above, the applicability of a micromorphic fluid as a model for human blood can be discussed. The analysis focuses on pipes with small radius, which represent simplified blood vessels. First, the relationship between experimental data and analytical solutions is discussed to facilitate a meaningful discussion of the results. Second, the results are compared to corresponding results from the literature (*cf.* [22]). Third, a new set of viscosity coefficients is derived from the Fåhræus–Lindqvist effect. Then, the resulting fluid model is compared to experimental data and, finally, the influence of several viscosity coefficients on the micromorphic fluid behavior is investigated.

The viscosity coefficients used in this section generally depend on the initial RBC hematocrit. A motivation for restrictions regarding their magnitude is given in [22] and briefly repeated in Sect. 3.3. Furthermore, the values for the coupling boundary condition in this section are specified in Eq. (3.6). Thus, the micromotion of the fluid at the wall is considered to be driven by the surrounding fluid motion, but also slowed down by particle–wall interaction and crowding effects.

4.1 Normalization of experimental data

As explained in Sect. 1, the viscosity μ of blood is not constant with respect to the vessel radius R, but decreases with decreasing radius for $R < 300$ μm, which corresponds to the well-known Fåhræus–Lindqvist effect (*cf.* [13]). In order to conduct a meaningful discussion, it is necessary to clarify how the fields are normalized. To achieve this, the apparent viscosity μ_{app} is reformulated in terms of the micromorphic viscosity coefficient μ from Eqs. (3.8) [22]:

$$\mu_{\text{app}} := -\frac{\pi R^4 P}{8Q} \qquad \Rightarrow \qquad \mu_{\text{app}} = \frac{\mu}{4\overline{Q}}, \tag{4.1}$$

where Q denotes the total volume flow rate, given by

$$Q = \iint_A \boldsymbol{v} \cdot \mathrm{d}\boldsymbol{A} = \iint_A \boldsymbol{v} \cdot \boldsymbol{e}_z \, \mathrm{d}A = \int_0^{2\pi} \int_0^R v(r) r \, \mathrm{d}r \, \mathrm{d}\varphi. \tag{4.2}$$

By using $\rho = r/R$ and $\mathrm{d}r = R \, \mathrm{d}\rho$, the volume flow rate can be written in terms of the dimensionless velocity from Eq. (3.11):

$$Q = \int_0^{2\pi} \int_0^1 R^2 v_0 \frac{v(\rho)}{v_0} \rho \, \mathrm{d}\rho \, \mathrm{d}\varphi = 2\pi R^2 v_0 \int_0^1 \frac{v(\rho)}{v_0} \rho \, \mathrm{d}\rho. \tag{4.3}$$

The remaining integral is denoted as $\overline{Q}$, which yields an adapted, dimensionless expression for the volume flow rate [22, p. 152]:

$$Q = 2\pi R^2 v_0 \overline{Q}, \qquad \overline{Q} = \int_0^1 \frac{v(\rho)}{v_0} \rho \, \mathrm{d}\rho. \tag{4.4}$$

For a Newtonian fluid, the apparent viscosity is constant, because the Newtonian volume flow rate Q is always proportional to PR^4. Consequently, $\overline{Q} = 1/4$ will always hold. Hence, the apparent viscosity can be interpreted as a measure for the change of the normalized volume flow rate for a varying radius. A variable apparent viscosity indicates a deviation from Newtonian behavior. To normalize the solution properly, the micromorphic viscosity coefficient μ can be set to a reference viscosity for all R. For instance, a suitable reference viscosity is the asymptotic value of approximately 3.77 mPa s obtained from experiments with large radii by [20].

By choosing v_0 as a function of a constant μ, the normalized volume flow rate $\overline{Q}$ for a micromorphic fluid will change with the vessel radius, because the normalized solution $v(\rho)/v_0$ still depends on R. The choice of a reference velocity of $\tilde{v}_0 = -PR^2/(4\mu_{\text{app}})$ with an experimentally obtained value of μ_{app} corresponds to a normalization by the experimental volumetrically averaged velocity v_{m}, see Eqs. (4.1, 4.4):

$$\frac{v(\rho)}{\tilde{v}_0} = -\frac{\mu}{4\overline{Q}}\frac{4}{PR^2}v(\rho) = \frac{v(\rho)}{2v_{\text{m}}}. \tag{4.5}$$

If the fluid model shows the same shear-thinning behavior as blood, the normalized volume flow rate will stay constant with varying radius. Thus, if the subsequently computed volume flow rate of $v(\rho)/\tilde{v}_0$ does change with R or dimensionless experimental data does not fit the model, it is an indication for a flawed model or wrongly chosen parameters.

4.2 Comparison to Kang and Eringen

The solution derived above is compared to the reference solution from Kang and Eringen [22]. In order to enable this comparison, all model parameters are matching those from the reference. The experimentally obtained apparent viscosity of blood specified in [19,21] for $R = 100\,\mu\text{m}$ was chosen for the micromorphic viscosity coefficient μ to compare velocity profiles at different R with each other and with experimental data. As explained above, this is a rather arbitrary and counter-intuitive choice for the viscosity, since it neither corresponds to the asymptotic nor the actual apparent viscosity at $R \in \{20\,\mu\text{m}, 35\,\mu\text{m}\}$. Due to the normalization with v_0 and thereby with μ, the choice of μ does not affect the velocity and micromotion profiles. Therefore, the values from [22] are adopted for now which includes the following viscosity coefficients:

$$\begin{aligned}
\mu &= 2.8\ \text{mPa s}, & \kappa/\mu &= 0.07, & \zeta_1/\mu &= -0.75, & \zeta_2/\mu &= 0.28, \\
K_1/\mu &= 1.1 \times 10^{-10}\,\text{m}^2, & K_2/\mu &= 1.0 \times 10^{-10}\,\text{m}^2, \\
K_3/\mu &= 0.9 \times 10^{-10}\,\text{m}^2, & K_4/\mu &= 0.6 \times 10^{-10}\,\text{m}^2.
\end{aligned} \tag{4.6}$$

There are two sign errors in the boundary values given in [22]. The first one was already outlined in "Appendix A" in Eq. (A.21): According to the coupling boundary from Eq. (3.5), the boundary condition should read

$$G_{(rz)}(R) = \lambda_2 d_{rz} = \lambda_2 \frac{v'(R)}{2} = \left(1 - \frac{5}{16}\text{Ht}\right)\frac{v'(R)}{2}, \tag{4.7a}$$

$$G_{[rz]}(R) = \lambda_3 w_{rz} = -\lambda_3 \frac{v'(R)}{2} = -(1 - \text{Ht})\left(1 - \frac{5}{16}\text{Ht}\right)\frac{v'(R)}{2}. \tag{4.7b}$$

This formulation was also used for the derivation of our solution. However, after substituting the coefficients λ_2 and λ_3 from [22, p. 151] into Eqs. (5.6) from [22], the boundary conditions read:

$$G_{(rz)}(R) = -\lambda_2 v'(R) = \left(1 - \frac{5}{16}\text{Ht}\right)\frac{v'(R)}{2}, \tag{4.8a}$$

$$G_{[rz]}(R) = \lambda_3 v'(R) = (1 - \text{Ht})\left(1 - \frac{5}{16}\text{Ht}\right)\frac{v'(R)}{2}. \tag{4.8b}$$

Comparison of Eqs. (4.7) and (4.8) reveals a sign error within the boundary condition for the microrotation in [22]. This sign error would result in a negative relation between the microrotation and the vorticity at the wall. Hence, the micro-rotation at the wall would not only be smaller than the corresponding vorticity due to
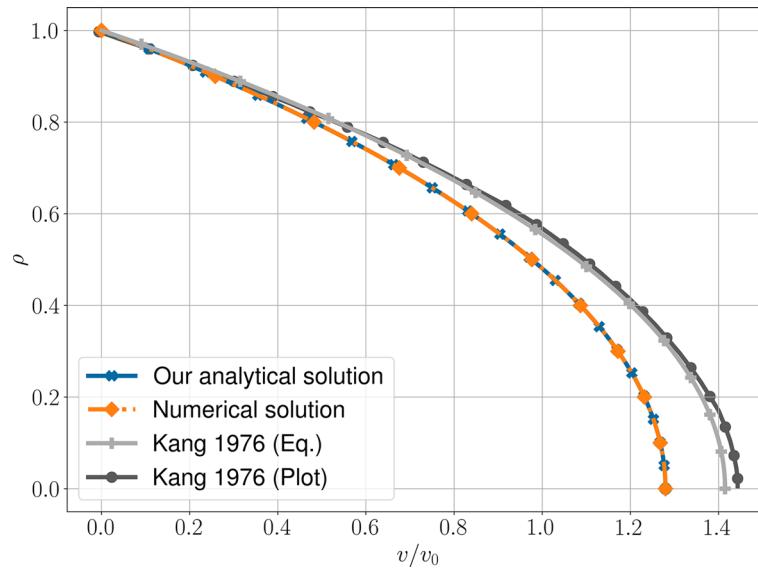
Fig. 2 Normalized velocity fields obtained for $R = 20\,\mu\text{m}$ and Ht $= 40\%$ compared to those provided by Kang and Eringen in mathematical and graphical form [22, pp. 149–151] using the flawed boundary condition, as outlined in Sect. 4.2

friction but also in the opposite direction. This behavior is not physically plausible and the formulation from [22] is therefore considered to be faulty.

The solutions to the BVP in Eq. (3.10) are exemplarily compared for $R = 20\,\mu\text{m}$. This comparison includes our analytical solution, the solutions published in [22], and a numerical solution. Before correcting the flawed boundary condition as described above, all solutions are compared for the physically implausible boundary condition stated by Kang and Eringen. It will be shown that our derived analytical solution does not coincide with the analytical solution from Kang and Eringen. Therefore, a numerical solution is used to validate our derived solution. This numerical solution was computed using the `NDSolve`-function of the *Mathematica* software, in which the three scalar PDEs along with the boundary conditions were specified. Next to the mathematical expression of the analytical solution, the velocity and the microrotation field were also plotted in by Kang and Eringen in Fig. 3, see [22, p. 151], which are also compared to the analytical solutions. The fact that these plotted solutions deviate from both analytical solutions indicates misprints or errors in [22]. Accordingly, the coupling parameters λ_2 and λ_3 will be corrected such that the physically meaningful boundary condition is prescribed, and the same comparison is performed again. After the adjustment, our analytical solution for the microrotation coincides with the plotted microrotation solution from Kang and Eringen, whereas their corresponding solution in mathematical form differs. For the velocity solution on the other hand, our validated analytical solution does neither match the graphical nor the analytical solution published in [22]. This leads to the conclusion that the analytical solutions from Kang and Eringen contain, first, misprints because their analytical solutions do not match their plotted solutions, and second, errors, since both their graphical and analytical solution for the velocity field differ from the correct solution to the BVP. The derivation of this conclusion is given in more detail below.

For the original boundary conditions from [22], the different velocity profiles are shown in Fig. 2, and the micromotion is displayed in Fig. 3. It is noticeable that the numerical results for all fields coincide with our derived solutions, whereas the analytical solution from Kang and Eringen deviates from them and—in the case of velocity and microrotation— from their plotted solution. For the microshearing, no graphical solution was provided by Kang and Eringen. Hence, our analytical solution solves the BVP, unlike the solutions from Kang and Eringen. The small difference between the analytical and graphical solution for the velocity field in [22] could originate from inaccuracies in plotting, and thus, no statement regarding the source of the difference to our solution can be made yet. In order to determine if a misprint in the boundary condition contributed to these differences, the flawed boundary condition is corrected and the solutions are compared again.

After correcting the boundary condition, differences between our analytical solutions and those from Kang and Eringen still exist, as depicted in Figs. 4 and 5. However, for the microrotation in Fig. 5b, the situation is different: The correction of the boundary conditions causes our solution and the plotted solution from Kang and Eringen to match, while their analytical solution still differs. Minor differences between our solution and
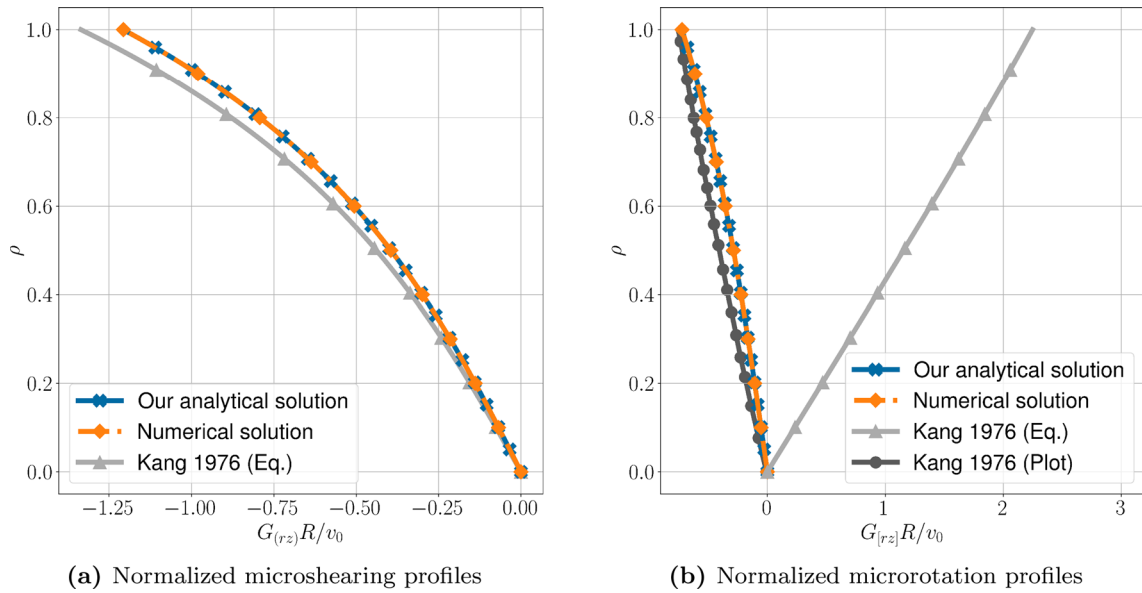
(a) Normalized microshearing profiles   **(b)** Normalized microrotation profiles

Fig. 3 Normalized micromotion fields obtained for $R = 20\,\mu m$ and $Ht = 40\%$ compared to those provided by Kang and Eringen in mathematical and graphical form [22, pp. 149–151] using the flawed boundary condition, as outlined in Sect. 4.2
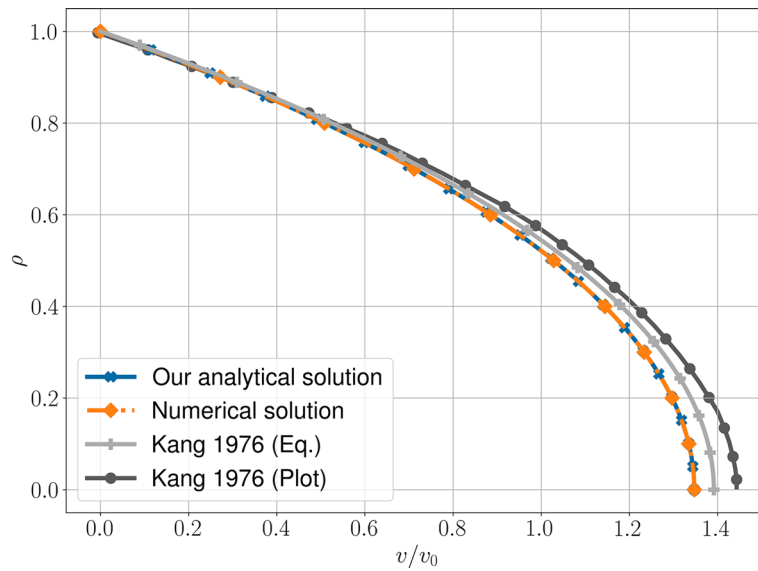

Fig. 4 Normalized velocity fields obtained for $R = 20\,\mu m$ and $Ht = 40\%$ compared to those provided by Kang and Eringen in mathematical and graphical form [22, pp. 149–151] using the corrected boundary condition, as outlined in Sect. 4.2

Kang and Eringen's graphical solution originate from the extraction of the graphical solution. It should also be noted that the plotted solution from [22] was negative for all ρ, whereas it should be positive for all ρ, at least when considering the correct boundary condition. For Fig. 5b, this error was treated by mirroring the graphical solution from [22]. The good accordance of our analytical with the graphical solution from Kang and Eringen indicates that the corrected coupling boundary condition indeed corresponds to the boundary condition they intended to use and that their analytical solution for the microrotation simply contains typographical errors. Regarding the velocity field, neither the mathematical expression nor the plot from [22] agrees with our validated solution. Thus, there is another error in the velocity solution that cannot be explained by a typographical error, although it could be due to the typographical error in the microrotation solution. For the microshearing it is similar: Albeit small, there is a difference between our validated analytical solution and the one from [22]. Consequently, the latter also contains errors.
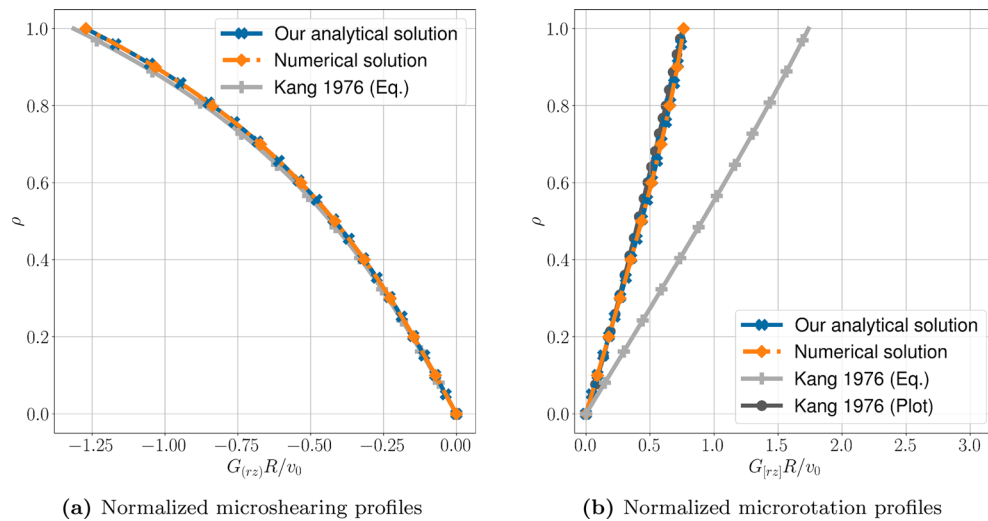
(a) Normalized microshearing profiles

(b) Normalized microrotation profiles

Fig. 5 Normalized micromotion fields obtained for $R = 20\,\mu\text{m}$ and $\text{Ht} = 40\%$ compared to those provided by Kang and Eringen in mathematical and graphical form [22, pp. 149–151] using the corrected boundary condition, as outlined in Sect. 4.2. The sign of the microrotation plot in [22] was changed for this figure, since it was negative for all ρ

To summarize, the solutions to the micromorphic pipe flow from Kang and Eringen contain several errors, as already stated. One error regarded the misprints in the solution for the microrotation, while the exact origin of the remaining errors could not be identified. Moreover, the analysis showed that the flawed boundary condition from [22] merely corresponds to a typographical error in the publication and that the physically meaningful boundary condition from Eqs. (4.7) was also considered by Kang and Eringen.

4.3 Derivation of model parameters

Due to the counter-intuitive choice of μ and the flawed equations in [22] which might have led to the viscosity coefficients from Eqs. (4.6), a new set of model parameters is derived based on experimental data. To acquire this new set of parameters, the apparent viscosity of a micromorphic fluid is fitted to the actual apparent viscosity of human blood with an initial hematocrit of 45%. The reference data were collected and aggregated in [27]. It comprises the results of 18 different studies of RBCs suspended in a Newtonian fluid with hematocrit values from 40% to 45%, where results with hematocrit less than 45% were extrapolated. Since the suspending fluid differed across the considered studies, an average for the relative apparent viscosity μ_rel, i.e., the apparent viscosity divided by the viscosity of the suspending fluid μ_s, was determined. From hereinafter the micromorphic viscosity μ denotes the asymptotic apparent viscosity as a function of μ_s under consideration of the results from [27]:

$$\mu := \mu_\text{s} \lim_{R \to \infty} \mu_\text{rel}(R), \qquad \mu \approx 3.23\mu_\text{s}. \qquad (4.9)$$

The fitting was conducted with the help of the `curve_fit` function from the python package `scipy.optimize`. This corresponds to applying the non-linear least-squares analysis to find a suitable set of parameters. The analysis was conducted for 19 data points in the range of radius from approximately 0.01mm to 2mm. For smaller vessel radii, the vessel dimension approximates the dimension of single RBCs, and the continuum approach ceases to be valid. The following bounds were imposed on the parameters according to the heuristics in [22]:

$$\kappa/\mu \in [0.05, 0.5], \qquad \zeta_1/\mu \in [-2, -1], \qquad \zeta_2/\mu \in [0.1, 1],$$
$$K_1/\mu \in [1 \times 10^{-10}\,\text{m}^2, 5 \times 10^{-10}\,\text{m}^2], \qquad K_2/\mu \in [1 \times 10^{-10}\,\text{m}^2, 5 \times 10^{-10}\,\text{m}^2],$$
$$K_3/\mu \in [-5 \times 10^{-10}\,\text{m}^2, -0.9 \times 10^{-10}\,\text{m}^2], \quad K_4/\mu \in [1.1 \times 10^{-10}\,\text{m}^2, 5 \times 10^{-10}\,\text{m}^2].$$
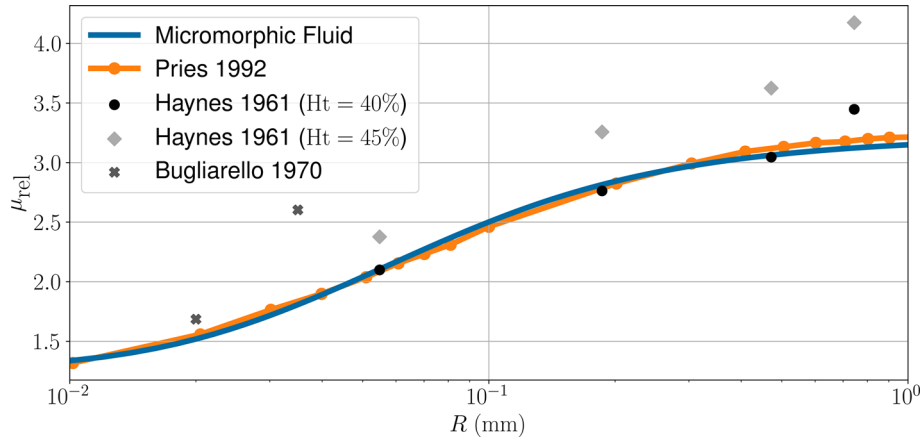
Fig. 6 Apparent viscosity of a micromorphic as compared to the experimental results published in [27] and [19]

The fitting resulted in the following set of parameters:

$$\kappa/\mu \approx 0.185, \qquad \zeta_1/\mu \approx -1.50, \qquad \zeta_2/\mu \approx 1.00,$$
$$K_1/\mu \approx 1.39 \times 10^{-10}\,\mathrm{m}^2, \qquad K_2/\mu \approx 1.00 \times 10^{-10}\,\mathrm{m}^2, \qquad (4.10)$$
$$K_3/\mu \approx -0.90 \times 10^{-10}\,\mathrm{m}^2, \qquad K_4/\mu \approx 5.00 \times 10^{-10}\,\mathrm{m}^2.$$

It should be noted that the values obtained for the aggregated gyration viscosity coefficients K_i as well as the coefficient ζ_2 approximately lie on their respective bounds. This indicates that the optimal values for K_i and ζ_2 lie beyond the imposed bounds. Nonetheless, for the following analysis the values from Eqs. 4.10 are considered.

4.4 Shear-thinning behavior of a micromorphic fluid

In this section, micromorphic fluid behavior is compared to the Fåhræus–Lindqvist effect. The asymptotic relative viscosity is computed for $R \in [10\,\mu\mathrm{m}, 1000\,\mu\mathrm{m}]$ and plotted against the experimental results from Pries et al. [27] and Haynes [19]. The former was used to determine the material parameters, while the latter served as reference data in the article from Kang and Eringen [22]. Since this analysis considers the relative instead of the absolute apparent viscosity, the results from [19] are normalized by the viscosity of the suspending fluid, i.e., Acid-Citrate-Dextrose (ACD). The different experimental results are not comparable one-to-one though, because the experiments in [19] were conducted for Ht $\in$ {0%, 20%, 30%, 40%, 50%, 60%, 70%, 80%}. Therefore, the results were interpolated to 45% quadratically. The resulting apparent viscosity is shown in Fig. 6. Additionally, the viscosity of two experiments conducted by Bugliarello and Sevilla [4] is included in the plot which are discussed in Sect. 4.5.

At first glance, it stands out how well the micromorphic relative apparent viscosity matches the actual relative apparent viscosity of RBC suspensions, as compiled in [27]. Clearly, this is due to the experimental data being used for the derivation of the model parameters, but the ability to reproduce the Fåhræus–Lindqvist effect at such accuracy is remarkable. It indicates that, for sufficiently high shear rates, a micromorphic fluid with the parameters from Eqs. (4.10), will exhibit nearly the same flow resistance as human blood in glass capillaries. However, for the micromorphic fluid to be a viable model for blood in microcirculation, it is not only required to follow the Fåhræus–Lindqvist effect, but also to resemble the actual motion of human blood. Consequently, the velocity distribution of a micromorphic fluid is investigated in the following section. Another interesting observation concerns the experimental results from Haynes [19]: At Ht = 40%, they coincide well with the data from Pries et al. [27], whereas they exceed the averaged values if interpolated to Ht = 45%. This strong variation across experimental data from literature was also pointed out in [27].
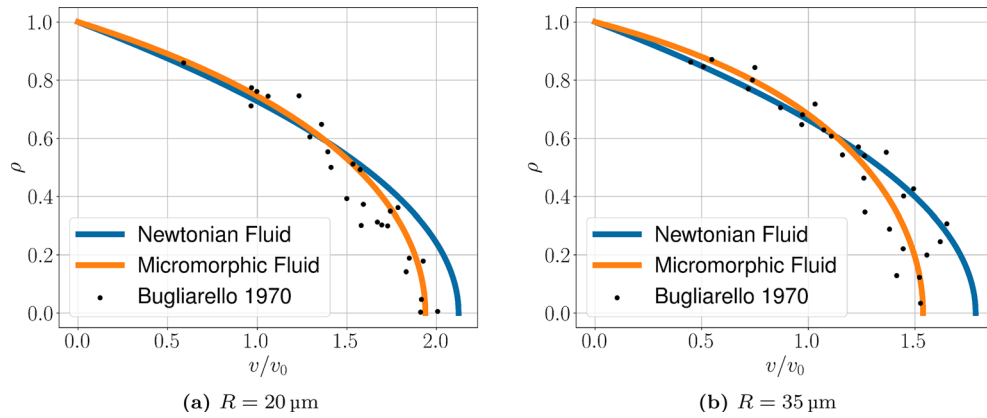
Fig. 7 Comparison of a micromorphic fluid and experimental data from [4] for different vessel radii

4.5 Comparison to experimental velocity profiles

In this section, several experimentally obtained velocity profiles of RBC suspensions in narrow glass capillaries are compared to those of a micromorphic fluid. This concerns data from Bugliarello and Sevilla [4] and Goldsmith and Marlow [15].

For $R \in \{20\,\mu\text{m}, 35\,\mu\text{m}\}$, a comparison with experimental data from Bugliarello and Sevilla [4] is possible. The experiments were conducted on a pressure-driven flow of RBCs suspended in ACD at Ht = 40%. Along with the absolute velocity, pressure-flow-diagrams were published, where the volume flow rate can be computed from the accompanying mean velocity v_m. This allows to determine v_0 which, in turn, allows for a normalization of given data. Since the published v_m does not agree with the respective velocity measurements, it is adjusted for the computation of v_0 (see "Appendix B"). Furthermore, the relative apparent viscosity was computed for both experiments using the ACD viscosity measured in [19] (see Fig. 6). Apparently, the relative apparent viscosity from the measured blood flows exceed the asymptotic relative apparent viscosity of human blood. Apart from noise, a possible explanation for the deviation is that the pseudo-shear rate $\overline{v}$ from Eq. (1.3) is too small for the apparent viscosity to tend to its asymptotic limit. Especially, for $R = 35\,\mu\text{m}$ with $\overline{v} \approx 17\,\text{s}^{-1}$, this is a plausible explanation. For $R = 20\,\mu\text{m}$ with $\overline{v} > 100\,\text{s}^{-1}$ on the other hand, the deviation should be negligible. In both cases, the normalization term v_0 was additionally shifted by the ratio of the different apparent viscosities. These two adjustments combined basically correspond to a normalization with respect to the volume flow rate. The resulting velocity profiles are shown in Fig. 7a, 7b.

Although the parameter optimization was only executed with respect to the apparent viscosity, the micromorphic velocity fields closely resemble the velocity fields of blood. This is especially noticeable if compared to a Newtonian velocity profile with the same volume flow rate: The micromorphic fluid exhibits the relatively blunted shape toward the vessel center, comparable to crowded RBCs forming a core region with smaller velocity differences. Near the vessel wall on the other hand, the velocity increases rapidly, similar to a friction-poor plasma layer.

Similar results are obtained from a comparison with experimental data from Goldsmith and Marlow [15], where the velocity fields of RBC and ghost cell suspensions were measured at $R \approx 40\,\mu\text{m}$ and varying hematocrit. Since in this case only a volume flow rate but no pressure gradient was given, the data are normalized to meet the volume flow rate of the micromorphic fluid. The resulting comparison is displayed in Fig. 8. Although the pseudo-shear rate $\overline{v}$ is below $50\,\text{s}^{-1}$ for all considered data sets, the general, blunted shape of the micromorphic and RBC suspension velocity profile is quite similar. Especially for an increasing pseudo-shear rate, the experimental data tends toward the micromorphic solution. However, it should also be noted that the volume flow rate of such low-shear experiments will most likely not agree with the micromorphic volume flow rate.

In conclusion, not only does the micromorphic fluid with adequately chosen parameters meet the Fåhræus–Lindqvist effect, but experimental velocity profiles can also be reproduced satisfactorily in a circular pipe flow. As to why micromorphic dynamics coincide with hemodynamics, and which parameters influence this behavior, will be investigated below.
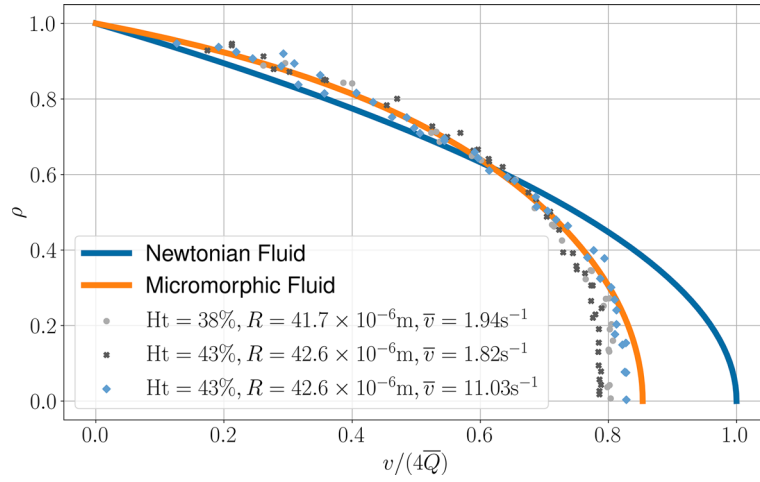
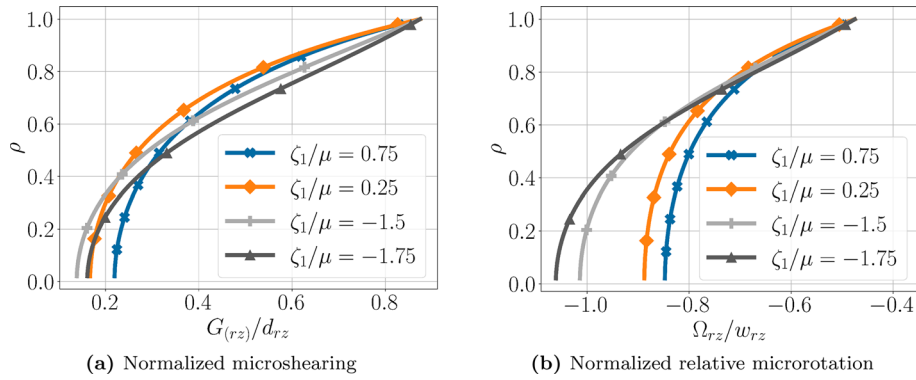**Fig. 8** Comparison of a micromorphic fluid and experimental data from [15] at $R \approx 40\,\mu m$

(a) Normalized microshearing

(b) Normalized relative microrotation

Fig. 9 Influence of ζ_1 on the normalized microshearing and relative microrotation of a micromorphic fluid in the microcirculation

4.6 Material parameter study

Using the derived material parameters from Eqs. (4.10), the micromorphic fluid motion resembles the motion of blood very well. Now, in order to get a better understanding of the associated material parameters, this section covers the influence of the viscosity coefficients contained in the stress tensor $\boldsymbol{t}$, namely κ and ζ_1, on the (micro-)motion and on the accompanying shear-thinning behavior. Of course, the viscosity μ is also included in $\boldsymbol{t}$, but a variation of μ will only affect the apparent viscosity, while it does not implicate a change within the normalized (micro-)motion.

For this study, the difference between vorticity and microrotation as well as the microshearing are of particular interest: Microrotations differing strongly from the surrounding fluid vorticity produce stress causing the fluid resistance to increase, while the microshearing and microstretching along the fluid shearing, i.e., the strain rate, causes stress reduction within the system. Therefore, the viscosity coefficients are varied around their optimized values, and the resulting change in relative apparent viscosity μ_{rel}, velocity v, microshearing $\mathrm{sym}(\boldsymbol{G})$, strain-rate $\boldsymbol{d}$, and relative microrotation $\boldsymbol{\Omega}$ is depicted. Here, the relative microrotation is defined as $\boldsymbol{\Omega}:=\mathrm{skw}(\boldsymbol{G}) - \boldsymbol{w}$. The parameter study regarding the field quantities is carried out at $R = 35\,\mu m$. For a variation of ζ_1, the micromotion results are presented in Fig. 9, where the microshearing and relative micromotion were normalized by the strain-rate and vorticity, respectively.

Varying ζ_1 has an insignificant effect on the normalized microshearing: Irrespective of ζ_1, it nearly vanishes in the RBC-rich core region, while stronger microshearing is induced in the high-shear area near the vessel wall. Thus, the ratio of strain-rate to micro-shearing is mostly independent of ζ_1. In contrast, the normalized relative microrotation is strongly influenced by a variation of ζ_1 in the core region: In relation to the fluid vorticity, decreasing ζ_1 also yields a decreasing relative microrotation. As for the microshearing, a variation
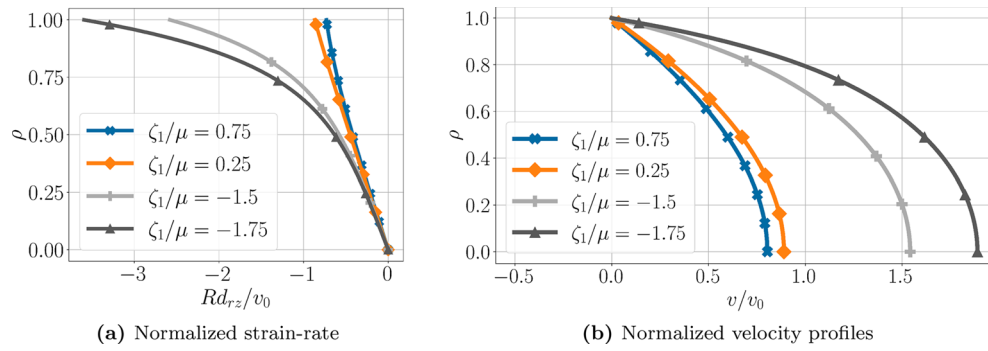
(a) Normalized strain-rate

(b) Normalized velocity profiles

Fig. 10 Influence of ζ_1 on the relative microshearing, relative microrotation, and velocity field of a micromorphic fluid in the microcirculation
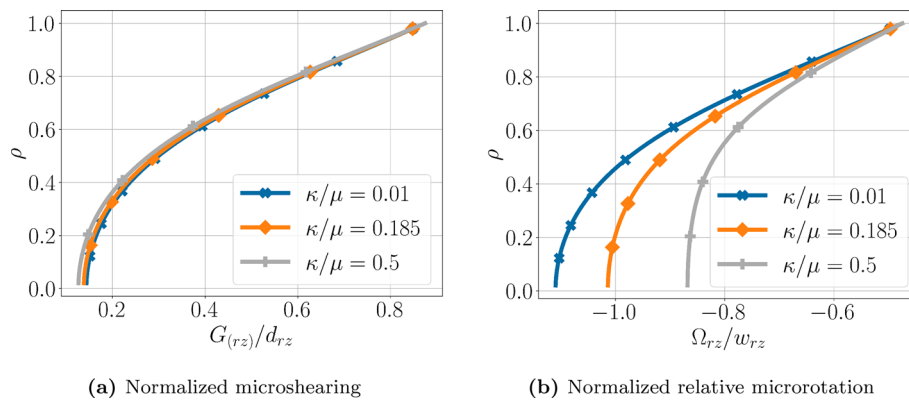

(a) Normalized microshearing

(b) Normalized relative microrotation

Fig. 11 Influence of κ on the microshearing and relative microrotation field of a micromorphic fluid in the microcirculation

of ζ_1 has a diminishing effect in the high-shear area close to the vessel wall. The concomitant change on the macro-scale fields is displayed in Fig. 10.

The strain-rate is simply increased in magnitude near the vessel wall for decreasing ζ_1, whereas the strain-rate in the inner vessel is only influenced marginally. Mathematically speaking, this is a consequence of ζ_1 directly influencing the Neumann boundary condition imposed on the velocity field. A possible interpretation can be inferred from the stress tensor t: ζ_1 governs the stress due to shearing on the micro-scale. In fact, Kang and Eringen state that higher $|\zeta_1|$, $|\zeta_2|$ correspond to more stress exerted on the system due to deformation, and thus, a "more flexible substructure," [22, p. 146]. However, since t is linear in ζ_1, changing the sign of ζ_1 also reverses the effect. For $\zeta_1 > 0$, the stress in the system due to microshearing along the strain rate is increased, while $\zeta_1 < 0$ induces stress relief as a consequence of microshearing along the strain rate. Hence, decreasing ζ_1 leads to a more flexible substructure. As a consequence, decreasing ζ_1 also leads to an increased velocity along the entire vessel.

Figure 11 shows how κ influences the micromotion: The variation of κ barely affects the normalized microshearing, while increasing κ results in a lower normalized relative microrotation, especially in the low-shear area near the vessel center. In the high shear flow near the vessel wall on the other hand, the microrotation-to-vorticity-ratio is mostly indifferent to a variation of κ due to the imposed boundary condition. The corresponding changes on the macroscopic field quantities are shown in Fig. 12. As a consequence of an increase in κ, the strain-rate declines, and the velocity diminishes. As visible in the formulation of the stress tensor t and as already stated in [22], large κ induce a high flow resistance due to particles rotating at a lower angular velocity than the surrounding vorticity field.

These phenomena can also be observed for the relative apparent viscosity, as shown in Fig. 13. An increase of ζ_1 leads to a less pronounced shear-thinning and even shear-thickening for $\zeta_1 > 0$. In a similar manner, higher values for κ damp the shear-thinning.

In conclusion, especially the negative material parameter ζ_1 governs the micromorphic shear-thinning behavior through stress reduction induced by particle deformation, whereas κ controls the stress due to differences between particle rotation and fluid vorticity. Hence, the micromorphic shear-thinning behavior is

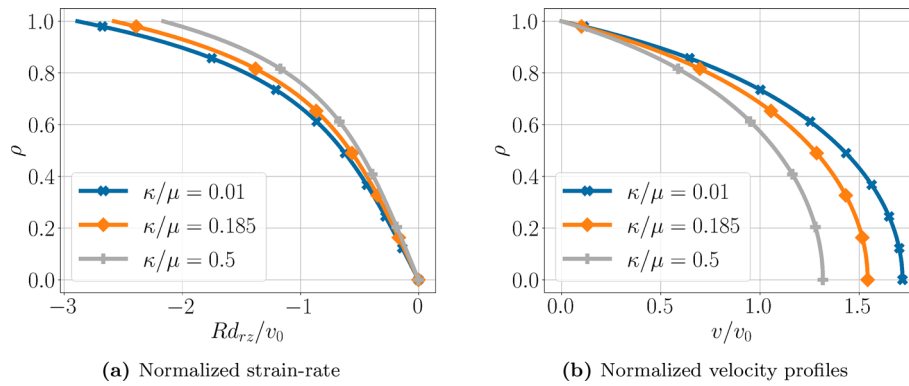**(a)** Normalized strain-rate

(b) Normalized velocity profiles

Fig. 12 Influence of κ on the strain-rate and velocity field of a micromorphic fluid in the microcirculation

(a) Relative apparent viscosity for variable ζ_1
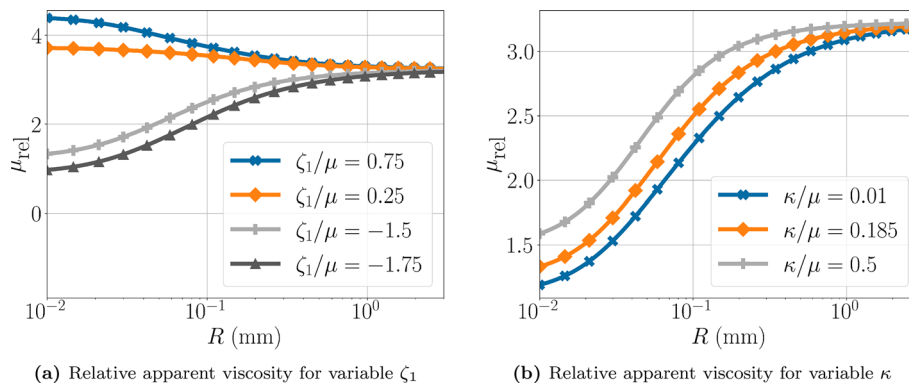
(b) Relative apparent viscosity for variable κ

Fig. 13 Influence of ζ_1 and κ on the relative apparent viscosity of a micromorphic fluid

determined by the flexibility on the micro-scale, as noted in [22]. Particle flexibility also corresponds to the actual cause for shear-thinning in blood [16]. For the given configuration, both stress reduction and stress build-up due to micromotion are mostly observed near the vessel wall. Moreover, the micromotion is only activated in areas with sufficiently high strain-rates, where the ratio of micromotion to strain-rate is always similar, irrespective of the chosen κ and ζ_1. This displays a major difference between micromorphic fluid behavior and hemodynamics: In actual blood, there is no particle deformation close to the wall, because there are no RBCs located close to the wall. However, Kang and Eringen motivate this discrepancy by an inverse relation between $\boldsymbol{\Omega}$ and the RBC-concentration: High magnitudes of $\boldsymbol{\Omega}$, i.e., a strong deviation of vorticity and microrotation, indicate that a particle has a greater sphere of influence, and thus, the local hematocrit must be lower.

4.7 Influence of varying vessel diameter

Regarding the motion on a macroscopic scale, the most distinguishing property of vertebrate blood compared to a Newtonian fluid is its shear-thinning behavior, i.e., the decrease of apparent viscosity μ_{app} along increasing strain-rate. As described in Sect. 1.1, the apparent viscosity of blood can be defined as a function of R, which, in turn, is satisfactorily modeled by a micromorphic fluid with our derived viscosity coefficients. This section is dedicated to analyzing the corresponding motion of a micromorphic fluid for varying vessel radii R. The considered vessel radii range from 10 µm to 500 µm to cover the full scope of microcirculation. In the former sections, it has already been shown that the velocity profile takes a more blunted shape than a Newtonian fluid. This evolution along varying R can be observed in Fig. 14 for the micromorphic fluid, where it was again put in context with a Newtonian fluid of the same normalized volume flow rate.

For large vessel radii, the micromorphic fluid almost fits the Newtonian fluid as expected, since here the inertial effects dominate the viscous effects of the material. From there, the micromorphic fluid profiles become more blunted until $R = 35$ µm, from where the trend retrieves until the velocity profile is almost parabolic
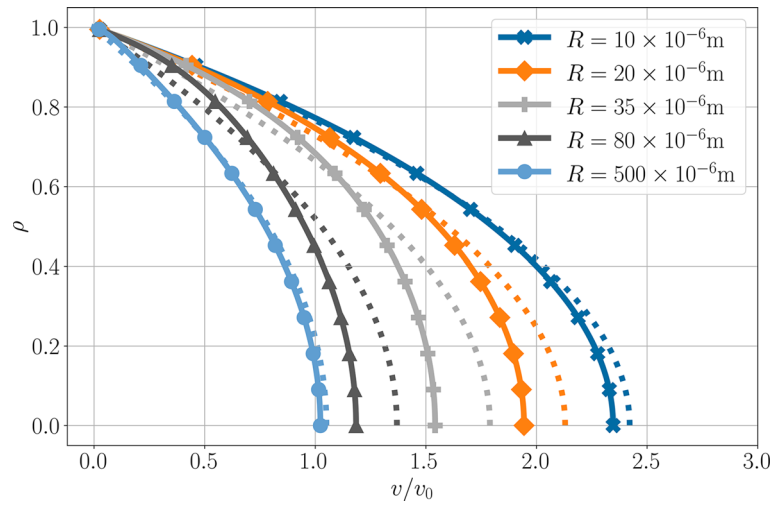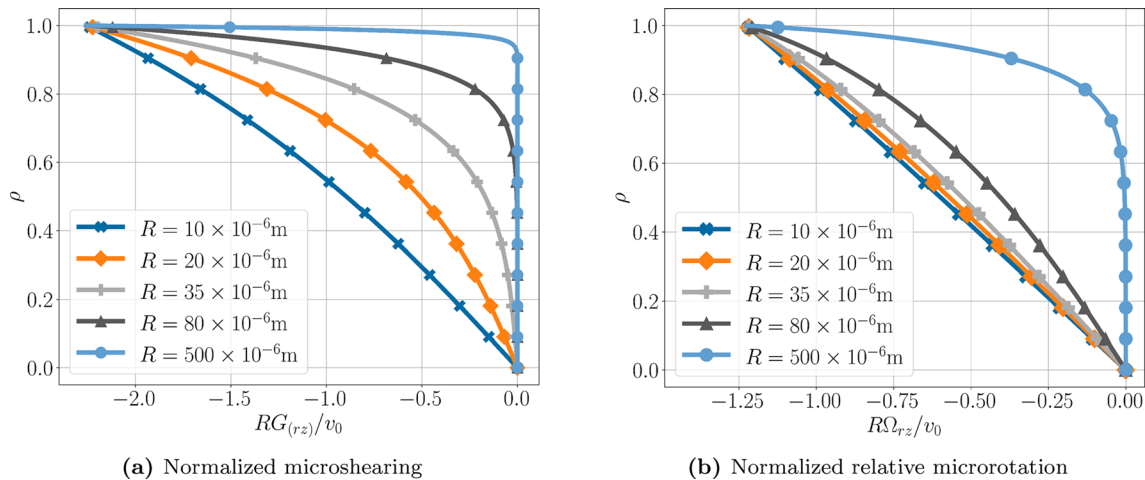
Fig. 14 Micromorphic velocity fields (solid line) for variable R as compared to a corresponding Newtonian velocity field (dotted line)

(a) Normalized microshearing

(b) Normalized relative microrotation

Fig. 15 Normalized (relative) micromotion fields for varying vessel radius R

again at $10\,\mu m$. It is not clear if this corresponds to the actual behavior of blood, or if the continuum approach ceases to be valid. More experimental data are required to validate the micromorphic approach as a model for blood in small vessels. In addition to the shape change, the normalized velocity profile also becomes steeper if the vessel diameter is decreased. The normalized volume flow rate $\overline{Q}$ is thereby increased. As a result, the volume flow rate Q is no longer proportional to PR^4, as it would be for a Newtonian fluid. This behavior corresponds to shear-thinning, or in the context of blood to the Fåhræus–Lindqvist effect. Since the origin of the micromorphic shear-thinning can be attributed to the micromotion, the evolution of the microshearing and the relative microrotation along varying vessel diameter is investigated below, see Fig. 15.

For decreasing vessel diameter, both the microshearing $G_{(rz)}$ and relative microrotation Ω_{rz} tend to a linear function. For large vessel radii beyond the scope of microcirculation on the other side, both $G_{(rz)}$ and Ω_{rz} vanish in the core region, but are increased in magnitude near the vessel wall abruptly. This agrees with the fact that blood can be considered a Newtonian fluid in large arteries. It also corresponds to the mechanism of the RBC-free, plasmatic layer in blood flow, whose thickness does not scale with the vessel radius [19,31]. The relative plasmatic layer thickness decreases along increasing vessel diameter, as does the micromotion's area of influence in Fig. 15. This behavior is also reflected in the strain-rate, as displayed in Fig. 16. For all radii but $R = 10\,\mu m$, the micromorphic fluid can be divided into a low-viscosity and high-viscosity area, indicated by the the steep strain-rate profile at the wall and the rather shallow profile in the core region, respectively. Just like the plasmatic layer, the relative thickness of the low-viscosity part shrinks with increasing vessel diameter.
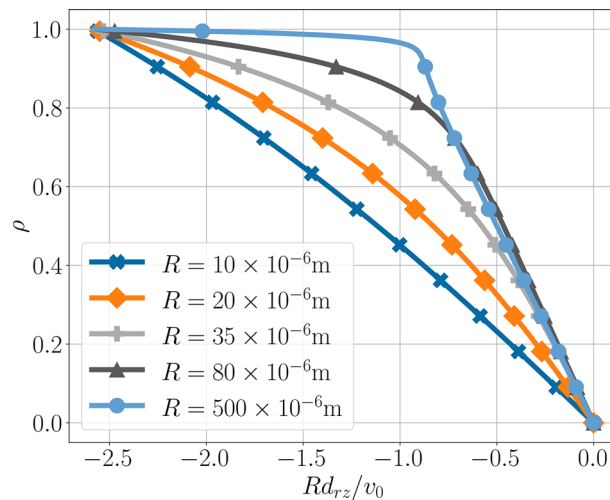
Fig. 16 Normalized strain-rate in a micromorphic fluid along variable R

Accordingly, the micromorphic velocity profiles match the blood profiles very well, as the comparison from Sect. 4.5 already showed.

5 Conclusion

While the calculations made in [22] partly contained misprints and the analysis was methodically flawed, the conclusions reached regarding the velocity profile and apparent viscosity are still valid: Experimental data is reproducible, shear-thinning occurs and even follows the Fåhræus–Lindqvist effect, while the reason for that, namely particle deformability, is even in accordance with the corresponding physical interpretation. Therefore, the so far studied effects indicate a high viability of a micromorphic fluid as a model for blood. However, there are more effects observed in blood, such as the evolution of the plasmatic layer size or the Fåhræus effect. They depend on the concentration, which is not a field quantity in micromorphic fluid theory. In order to study these effects anyway, Kang and Eringen derived a formulation for the RBC-concentration as a field quantity. This formulation is based on energy dissipation due to particle rotation and fluid shear in the presence of particles (cf. [18,35]). Since the particles were considered to be rigid and spherical, this analysis is not error-free applicable to a fluid model that considers a deformable microstructure. Therefore, it is not included here. But the approach could be used to compute the concentration of a microfluid with a microstructure of rigid, spherical particles, such as Eringen's micropolar fluid [9].

Despite the good results, the theory of micromorphic fluids is complex in that it introduces nine additional kinematic degrees of freedom and several additional viscosity coefficients compared to a Newtonian fluid. Hence, it is mathematically viable, and the linear stress tensor is a great advantage toward many popular models for blood depending on a strain-rate measure $\dot{\gamma} = \sqrt{2\mathbf{d} \cdot\cdot \mathbf{d}}$, see [30] for a comprehensive review. Such models including a nonlinear stress tensor easily result in numerical complications and restrictions. However, simulating a micromorphic fluid numerically can also result in a large model, requiring a lot of processing power and memory. In addition, the determination of more than 20 material parameters is a complicated task that requires a lot of reference data. Especially for blood, acquiring a large amount of data proves to be difficult, because the suspended particles are not translucent. Thus, a first step would be the model reduction to identify and discard redundant and unnecessary terms, in particular with regard to the first stress moments tensor, which alone contains 15 gyration viscosity coefficients. Unfortunately, this task again requires a lot of experimental data. Therefore, a less complex model, such as a modified micropolar fluid model, is desired to accurately compute blood flow in micro-circulation.

A Derivation of the micromorphic pipe flow

A.1 Evaluation of the momentum equation

Applying the product rule to the momentum equation in Eq. (2.2) yields a simple Ordinary Differential Equation (ODE):

$$\nabla \cdot \boldsymbol{t} = \boldsymbol{0} \tag{A.1a}$$

$$\Leftrightarrow \left(\frac{\partial t_{rz}}{\partial r} + \frac{1}{r} t_{rz} + \frac{\partial t_{zz}}{\partial z} \right) \boldsymbol{e}_z + \frac{\partial t_{rr}}{\partial r} \boldsymbol{e}_r = \boldsymbol{0}, \quad \text{where} \quad \frac{\partial t_{zz}}{\partial z} = \frac{\partial p}{\partial z} \tag{A.1b}$$

$$\Rightarrow \quad t'_{rz} + \frac{1}{r} t_{rz} = \frac{\partial p}{\partial z}, \qquad \frac{\partial p}{\partial r} = 0. \tag{A.1c}$$

Here the thermodynamic pressure was replaced by the hydrostatic pressure because of $-p\boldsymbol{1} = \boldsymbol{t}^\circ$, where the superscript circle denotes the spherical part of $\boldsymbol{t}$, i.e., the thermodynamic pressure. In addition to the ODE in Eqs. (A.1c), the second equation reveals information about the pressure:

$$p := p(z).$$

Hence, the ODE in Eq. (A.1c) is solved by

$$t_{rz} = \frac{r}{2} \frac{\partial p}{\partial z} + \frac{C_1}{r}. \tag{A.2}$$

For the sake of readability, the pressure gradient in z will hereinafter be referred to as $P := \partial p / \partial z$. Substituting the rz-component of the stress tensor $\boldsymbol{t}$, as displayed in Eq. (3.7a), in the ODE, yields

$$\left(\mu + \frac{\kappa}{2} \right) v'(r) + \zeta_1 \frac{G_{rz}(r) + G_{zr}(r)}{2} + \kappa \frac{G_{rz}(r) - G_{zr}(r)}{2} = \frac{r P}{2} + \frac{C_1}{r}, \tag{A.3}$$

where the constant C_1 must vanish due to the regularity requirement at $r = 0$. The obtained equation corresponds to Eq. (5.3a) from [22, p. 148]. Rewriting the expression leads to a function describing the velocity gradient in terms of the micro-rotation, the micro-stretching and the pressure gradient:

$$v'(r) = \frac{1}{\mu + \kappa/2} \left(\frac{r P}{2} - \zeta_1 \frac{G_{rz}(r) + G_{zr}(r)}{2} - \kappa \frac{G_{rz}(r) - G_{zr}(r)}{2} \right). \tag{A.4}$$

A.2 Evaluation of the micro-spin balance

The separate parts of the micro-spin balance (2.3) under consideration of Eq. (3.7) read

$$
\begin{aligned}
\nabla \cdot \overset{(3)}{\boldsymbol{\lambda}} =\ & \left[\gamma_1 \left(G''_{zr} + \frac{G'_{zr}}{r} - \frac{G_{zr}}{r^2} \right) + \gamma_2 \left(G''_{rz} + \frac{G'_{rz}}{r} - \frac{G_{rz}}{r^2} \right) \right] \boldsymbol{e}_r \otimes \boldsymbol{e}_z \\
& + \left[\gamma_4 \left(G''_{zr} + \frac{G'_{zr}}{r} - \frac{G_{zr}}{r^2} \right) + \gamma_5 \left(G''_{rz} + \frac{G'_{rz}}{r} - \frac{G_{rz}}{r^2} \right) \right] \boldsymbol{e}_z \otimes \boldsymbol{e}_r \\
& + \gamma_{10} \left[G''_{rz} + \frac{G'_{rz}}{r} - \frac{G_{rz}}{r^2} \right] \boldsymbol{e}_z \otimes \boldsymbol{e}_r + \gamma_{11} \left[G''_{rz} + \frac{G'_{rz}}{r} - \frac{G_{rz}}{r^2} \right] \boldsymbol{e}_r \otimes \boldsymbol{e}_z \\
& + \gamma_{12} \left[G''_{zr} + \frac{G'_{zr}}{r} - \frac{G_{zr}}{r^2} \right] \boldsymbol{e}_z \otimes \boldsymbol{e}_r + \gamma_{13} \left[G''_{zr} + \frac{G'_{zr}}{r} - \frac{G_{zr}}{r^2} \right] \boldsymbol{e}_r \otimes \boldsymbol{e}_z \\
& + \gamma_{14} \left[G''_{rz} + \frac{G'_{rz}}{r} - \frac{G_{rz}}{r^2} \right] \boldsymbol{e}_r \otimes \boldsymbol{e}_z + \gamma_{14} \left[G''_{zr} + \frac{G'_{zr}}{r} - \frac{G_{zr}}{r^2} \right] \boldsymbol{e}_z \otimes \boldsymbol{e}_r \\
& + \gamma_{15} \left[G''_{rz} + \frac{G'_{rz}}{r} - \frac{G_{rz}}{r^2} \right] \boldsymbol{e}_z \otimes \boldsymbol{e}_r + \gamma_{15} \left[G''_{zr} + \frac{G'_{zr}}{r} - \frac{G_{zr}}{r^2} \right] \boldsymbol{e}_r \otimes \boldsymbol{e}_z
\end{aligned}
\tag{A.5}
$$

and

$$
\begin{aligned}
\boldsymbol{t} - \boldsymbol{s} =\ & (\zeta_1 - 2\zeta_2) \frac{G_{rz} + G_{zr}}{2} (\boldsymbol{e}_r \otimes \boldsymbol{e}_z + \boldsymbol{e}_z \otimes \boldsymbol{e}_r) \\
& + \frac{\kappa}{2} (G_{rz} - G_{zr} + v')(\boldsymbol{e}_r \otimes \boldsymbol{e}_z - \boldsymbol{e}_z \otimes \boldsymbol{e}_r).
\end{aligned}
\tag{A.6}
$$

Plugging these into the micro-spin balance (2.3) yields the following system of differential equations from the rz- and zr-component:

$$
\begin{aligned}
& k_1 \left(G''_{zr} + \frac{G'_{zr}}{r} - \frac{G_{zr}}{r^2} \right) + k_2 \left(G''_{rz} + \frac{G'_{rz}}{r} - \frac{G_{rz}}{r^2} \right) \\
& + \frac{\zeta_1 - 2\zeta_2}{2} (G_{rz} + G_{zr}) + \frac{\kappa}{2} (G_{rz} - G_{zr} + v') = 0,
\end{aligned}
\tag{A.7a}
$$

$$
\begin{aligned}
& k_3 \left(G''_{zr} + \frac{G'_{zr}}{r} - \frac{G_{zr}}{r^2} \right) + k_4 \left(G''_{rz} + \frac{G'_{rz}}{r} - \frac{G_{rz}}{r^2} \right) \\
& + \frac{\zeta_1 - 2\zeta_2}{2} (G_{rz} + G_{zr}) - \frac{\kappa}{2} (a - G_{zr} + v') = 0,
\end{aligned}
\tag{A.7b}
$$

where the different k_i summarize gyration viscosity coefficients:

$$
\begin{aligned}
k_1 &= \gamma_1 + \gamma_{13} + \gamma_{15}, & k_2 &= \gamma_2 + \gamma_{11} + \gamma_{14}, \\
k_3 &= \gamma_4 + \gamma_{12} + \gamma_{14}, & k_4 &= \gamma_5 + \gamma_{10} + \gamma_{15}.
\end{aligned}
$$

This system of differential equations still depends on $v'(r)$, $G_{rz}(r)$, $G_{zr}(r)$ and P. Thus, Eq. (A.4) is substituted in the PDEs in order to eliminate $v'(r)$ and decouple the micro-spin balance from the momentum equation. Adding and subtracting Eqs. (A.7) afterwards yields

$$
\begin{aligned}
K_1 & \left(G''_{zr}(r) + \frac{G'_{zr}(r)}{r} - (\alpha_1^2 + r^{-2}) G_{zr}(r) \right) \\
& + K_2 \left(G''_{rz}(r) + \frac{G'_{rz}(r)}{r} - (\alpha_2^2 + r^{-2}) G_{rz}(r) \right) = 0,
\end{aligned}
\tag{A.8a}
$$

$$
\begin{aligned}
K_3 & \left(G''_{zr}(r) + \frac{G'_{zr}(r)}{r} - (\alpha_3^2 + r^{-2}) G_{zr}(r) \right) \\
& + K_4 \left(G''_{rz}(r) + \frac{G'_{rz}(r)}{r} - (\alpha_4^2 + r^{-2}) G_{rz}(r) \right) = -\frac{\kappa r P}{2\mu + \kappa},
\end{aligned}
$$

$$(A.8b)$$

where the different K_i consists of the gyration viscosity coefficients

$$K_1 = \gamma_1 + \gamma_{13} + \gamma_{15} + \gamma_4 + \gamma_{12} + \gamma_{14}, \tag{A.9a}$$
$$K_2 = \gamma_2 + \gamma_{11} + \gamma_{14} + \gamma_5 + \gamma_{10} + \gamma_{15}, \tag{A.9b}$$
$$K_3 = \gamma_1 + \gamma_{13} + \gamma_{15} - (\gamma_4 + \gamma_{12} + \gamma_{14}), \tag{A.9c}$$
$$K_4 = \gamma_2 + \gamma_{11} + \gamma_{14} - (\gamma_5 + \gamma_{10} + \gamma_{15}), \tag{A.9d}$$

while the α_i^2 are composed of the summarized viscosity coefficients:

$$\alpha_1^2 = -(\zeta_1 - 2\zeta_2)/K_1, \qquad\qquad \alpha_2^2 = -(\zeta_1 - 2\zeta_2)/K_2 \tag{A.10a}$$
$$\alpha_3^2 = -\kappa(2\mu + \zeta_1)/(K_3(2\mu + \kappa)), \quad \alpha_4^2 = \kappa(2\mu - \zeta_1)/(K_4(2\mu + \kappa)). \tag{A.10b}$$

The expressions for α_i^2 are adopted from [22], and Eqs. (A.8) correspond to Eqs. (5.3b)-(5.3c) in [22, p. 148]. In the following, these derived equations are used for finding a solution for the gyration tensor as well as for the velocity field. This section concerns the solution of the above-derived BVP. The derived and partially decoupled field equations are solved below, starting with the solution for G, which yields the velocity solution after a simple integration.

A.3 Solution for the micro-motion

In order to solve Eqs. (A.8), the homogeneous problem is considered first, and the inhomogeneous problem is solved afterwards to obtain a general solution. Finally, the boundary conditions are applied to find the specific solution.

A.3.1 Homogeneous solution

The different expressions in Eqs. (A.8) are similar to the modified Bessel differential equation

$$x^2 f''(x) + x f'(x) - (x^2 + n^2) f(x) = 0, \tag{A.11}$$

which is solved by the modified Bessel functions of the first and second kind. Therefore, the following ansatz is made:

$$G_{rz}(r) = C I_1(\alpha r) + \hat{C} K_1(\alpha r), \tag{A.12a}$$
$$G_{zr}(r) = D I_1(\beta r) + \hat{D} K_1(\beta r). \tag{A.12b}$$

Here, $I_n(x)$ and $K_n(x)$ denote the Bessel functions of the first and second kind, respectively. Since $K_n(\alpha r)$ is not defined for $r = 0$, and the solution requires to be defined for all $r \in \overline{\Omega}$, $\hat{C} = \hat{D} = 0$ can be concluded. In order to solve the homogeneous problem, the ansatz function is substituted in Eq. (A.11) using the linear coordinate transformation $x(r) = \alpha r$ with

$$\frac{\partial}{\partial r} f(x(r)) = \frac{\partial f(x(r))}{\partial x} \frac{\partial x}{\partial r}$$
$$\Leftrightarrow \quad \frac{\partial f(\alpha r)}{\partial r} = \alpha \frac{\partial f(x)}{\partial x}$$
$$\Leftrightarrow \quad \frac{1}{\alpha} f'(\alpha r) = f'(x)$$

and analogously

$$\frac{1}{\alpha^2} f''(\alpha r) = f''(x).$$

The modified Bessel differential equation can thereby be rewritten as

$$x^2 I_1''(x) + x I'(x) - (x^2 + 1) I_1(x) = 0 \tag{A.13a}$$

$$\Leftrightarrow I_1''(x) + x^{-1} I_1'(x) - (1 + x^{-2}) I_1(x) = 0 \tag{A.13b}$$

$$\Leftrightarrow \frac{1}{\alpha^2} I_1''(\alpha r) + \frac{1}{\alpha^2 r} I_1'(\alpha r) - \left(1 + \frac{1}{\alpha^2 r^2}\right) I_1(\alpha r) = 0 \tag{A.13c}$$

$$\Leftrightarrow I_1''(\alpha r) + \frac{1}{r} I_1'(\alpha r) - \left(\alpha^2 + \frac{1}{r^2}\right) I_1(\alpha r) = 0 \tag{A.13d}$$

$$\Leftrightarrow I_1''(\alpha r) + \frac{1}{r} I_1'(\alpha r) - \left(\alpha_i^2 + \frac{1}{r^2}\right) I_1(\alpha r) = (\alpha^2 - \alpha_i^2) I_1(\alpha r). \tag{A.13e}$$

The identity from Eq. (A.13e) is used to transfer the system of PDEs into a system of linear equations:

$$(\alpha^2 - \alpha_1^2) K_1 D I_1(\alpha r) + (\beta^2 - \alpha_2^2) K_2 C I_1(\beta r) = 0, \tag{A.14a}$$

$$(\alpha^2 - \alpha_3^2) K_3 D I_1(\alpha r) + (\beta^2 - \alpha_4^2) K_4 C I_1(\beta r) = 0. \tag{A.14b}$$

The power series representation of the Bessel function of the first kind is given by:

$$I_n(z) = \left(\frac{z}{2}\right)^n \sum_{k=0}^{\infty} \frac{\left(\frac{z}{2}\right)^{2k}}{k!(n+k)!}$$

If this power series is substituted in Eq. (A.14)), according to the identity theorem for polynomials, the PDE can only be fulfilled for all $k \in \mathbb{N}$ if the equalities

$$(\alpha^2 - \alpha_1^2) K_1 D \left(\frac{\alpha r}{2}\right)^{2k+1} + (\beta^2 - \alpha_2^2) K_2 C \left(\frac{\beta r}{2}\right)^{2k+1} = 0 \tag{A.15}$$

$$(\alpha^2 - \alpha_3^2) K_3 D \left(\frac{\alpha r}{2}\right)^{2k+1} + (\beta^2 - \alpha_4^2) K_4 C \left(\frac{\beta r}{2}\right)^{2k+1} = 0 \tag{A.16}$$

hold true. These two equations can only be fulfilled for all k if $\alpha = \beta$. The homogeneous problem can therefore be expressed as following system of linear equations:

$$\left(K_1(\alpha^2 - \alpha_1^2) D + K_2(\alpha^2 - \alpha_2^2) C\right) I_1(\alpha r) = 0, \tag{A.17a}$$

$$\left(K_3(\alpha^2 - \alpha_3^2) D + K_4(\alpha^2 - \alpha_4^2) C\right) I_1(\alpha r) = 0, \tag{A.17b}$$

$$\Leftrightarrow \underbrace{\begin{pmatrix} (\alpha^2 - \alpha_1^2) K_1 & (\alpha^2 - \alpha_2^2) K_2 \\ (\alpha^2 - \alpha_3^2) K_3 & (\alpha^2 - \alpha_4^2) K_4 \end{pmatrix}}_{=:\mathbf{A}} \begin{pmatrix} D \\ C \end{pmatrix} = \mathbf{0}. \tag{A.17c}$$

Since Eq. (A.17c) is a homogeneous system of linear equations, the rows must depend on each other, which is fulfilled if the determinant of $\mathbf{A}$ vanishes. Otherwise, the solution to the linear equation system would be the trivial solution, i.e., $C = D = 0$. Hence, the solution to the homogeneous system of differential equations is found by adding the two linear independent solutions

$$G_{rz}(r) = C_1 I_1(\alpha r) + C_2 I_1(\beta r), \tag{A.18a}$$

$$G_{zr}(r) = D_1 I_1(\alpha r) + D_2 I_1(\beta r), \tag{A.18b}$$

where α and β can be obtained from solving

$$\det(\mathbf{A}) = (\lambda_{1/2}^2 - \alpha_1^2)(\lambda_{1/2}^2 - \alpha_4^2) K_1 K_4 - (\lambda_{1/2}^2 - \alpha_2^2)(\lambda_{1/2}^2 - \alpha_3^2) K_2 K_3 \overset{!}{=} 0$$

Finally, after plugging Eqs. (A.18) into Eq. (A.8a), one obtains the following relations between C_i and D_i:

$$f_1 := \frac{D_1}{C_1} = -\frac{(\alpha^2 - \alpha_2^2)}{(\alpha^2 - \alpha_1^2)} \frac{K_2}{K_1}, \quad f_2 := \frac{D_2}{C_2} = -\frac{(\beta^2 - \alpha_2^2)}{(\beta^2 - \alpha_1^2)} \frac{K_2}{K_1}. \tag{A.19}$$

A.3.2 Inhomogeneous solution

Since the right-hand side of Eqs. (A.8) also contains an inhomogeneous part, the inhomogeneous problem must be solved as well. The solution of the inhomogeneous problem is called particular solution, in the following denoted by the subscript p, whereas the homogeneous solution is denoted by the subscript h. The final solution is obtained by adding the homogeneous and particular solutions:

$$G_{rz} = G_{rz,\mathrm{h}} + G_{rz,\mathrm{p}}, \qquad G_{zr} = G_{zr,\mathrm{h}} + G_{zr,\mathrm{p}}.$$

By inspecting this inhomogeneous part of Eqs. (A.8), it can be deduced that linear terms in $G_{rz,\mathrm{p}} = Ar$ and $G_{zr,\mathrm{p}} = Br$ solve the inhomogeneous PDEs, because the second derivatives vanish, while the first derivatives are eliminated. This leaves the following system of equations to be solved:

$$-K_1 \alpha_1^2 Ar - K_2 \alpha_2^2 Br = 0,$$

$$-K_3 \alpha_3^2 Ar - K_4 \alpha_4^2 Br = -\frac{\kappa r P}{2\mu + \kappa}.$$

As a consequence of the definitions of α_i^2 (Eqs. (A.10)), the following equations are obtained to solve the inhomogeneous BVP:

$$G_{rz}(r) = C_1 I_1(\alpha r) + C_2 I_1(\beta r) - \frac{P}{4\mu} r, \tag{A.20a}$$

$$G_{zr}(r) = f_1 C_1 I_1(\alpha r) + f_2 C_2 I_1(\beta r) + \frac{P}{4\mu} r. \tag{A.20b}$$

A.3.3 Specific solution

To find the specific solution of the system of PDEs (A.8), one needs to substitute the boundary conditions into Eqs. (A.20) and solve them for C_1, C_2. Hence, the equality

$$\frac{G_{rz}(R) + G_{zr}(R)}{2} = \lambda_2 \frac{v'(R)}{2}, \quad \frac{G_{rz}(R) - G_{zr}(R)}{2} = -\lambda_3 \frac{v'(R)}{2} \tag{A.21}$$

must hold. Note that there is a deviation toward [22], where a mix-up regarding both signs within the boundary conditions seems to have happened. Furthermore, in [22] the right-hand side is missing the factor $1/2$, because it is contained in λ_2, λ_3. Substituting these relations in Eq. (A.3) yields

$$v'(R) = \frac{RP}{2} \Big/ \left(\mu + \frac{\kappa}{2} + \frac{\lambda_2 \zeta_1}{2} - \frac{\lambda_3 \kappa}{2} \right), \tag{A.22}$$

which corresponds to a Neumann boundary for v and thereby to a Dirichlet boundary for G_{rz} and G_{zr}. Now define $L := \alpha R$, $M := \beta R$ and evaluate Eqs. (A.20):

$$\begin{aligned}
G_{rz}(R) + G_{zr}(R) &= C_1 \left(1 + f_1\right) I_1(L) + \\
&\quad + C_2 \left(1 + f_2\right) I_1(M) = \lambda_2 v'(R), \\
G_{rz}(R) - G_{zr}(R) &= C_1 \left(1 - f_1\right) I_1(L) + \\
&\quad + C_2 \left(1 - f_2\right) I_1(M) - \frac{PR}{2\mu} = -\lambda_3 v'(R)
\end{aligned} \tag{A.23}$$

Again, the equations can be transformed into a system of linear equations

$$\begin{pmatrix} (1 + f_1) & (1 + f_2) \\ (1 - f_1) & (1 - f_2) \end{pmatrix} \begin{pmatrix} C_1 I_1(L) \\ C_2 I_1(M) \end{pmatrix} = \begin{pmatrix} \lambda_2 v'(R) \\ -\lambda_3 v'(R) + \frac{PR}{2\mu} \end{pmatrix},$$

which is solved by inverting the system matrix:

$$\begin{pmatrix} C_1 I_1(L) \\ C_2 I_1(M) \end{pmatrix} = \frac{1}{2(f_1 - f_2)} \begin{pmatrix} (1 - f_2) & -(1 + f_2) \\ -(1 - f_1) & (1 + f_1) \end{pmatrix} \begin{pmatrix} \lambda_2 v'(R) \\ -\lambda_3 v'(R) + \frac{PR}{2\mu} \end{pmatrix}$$

This inversion is only possible if $f_1 \neq f_2$, thus, if $K_1 \neq K_2$. The constants C_1, C_2 can therefore be expressed as

$$C_1 = \frac{(1 - f_2)\lambda_2 v'(R) + (1 + f_2)\lambda_3 v'(R) - 2(1 + f_2)\frac{PR}{4\mu}}{2I_1(L)(f_1 - f_2)}, \quad (A.24a)$$

$$C_2 = \frac{(f_1 - 1)\lambda_2 v'(R) - (1 + f_1)\lambda_3 v'(R) + 2(1 + f_1)\frac{PR}{4\mu}}{2I_1(M)(f_1 - f_2)}. \quad (A.24b)$$

In order to obtain a dimensionless solution, the constants can also be rewritten in terms of the normalization velocity $v_0 := - PR^2/(4\mu)$, as suggested in [22]:

$$C_{1\star} := \frac{C_1 R}{v_0} = \frac{(f_2 - 1)\mu/a\lambda_2 - (1 + f_2)\mu/a\lambda_3 + (1 + f_2)}{I_1(L)(f_1 - f_2)}, \quad (A.25a)$$

$$C_{2\star} := \frac{C_2 R}{v_0} = \frac{(1 - f_1)\mu/a\lambda_2 + (1 + f_1)\lambda_3\mu/a - (1 + f_1)}{I_1(M)(f_1 - f_2)}, \quad (A.25b)$$

where the dimensionless wall velocity gradient can be expressed using

$$\frac{Rv'(R)}{v_0} = -2\mu/a, \qquad a := \mu + \frac{\kappa}{2} + \frac{\lambda_2\zeta_1}{2} - \frac{\lambda_3\kappa}{2}. \quad (A.26)$$

Hence, the normalized microrotation and microshearing are expressed as

$$\frac{R}{v_0}G_{(rz)}(\rho) = \frac{C_{1\star}}{2}(1 + f_1)I_1(L\rho) + \frac{C_{2\star}}{2}(1 + f_2)I_1(M\rho), \quad (A.27a)$$

$$\frac{R}{v_0}G_{[rz]}(\rho) = \rho + \frac{C_{1\star}}{2}(1 - f_1)I_1(L\rho) + \frac{C_{2\star}}{2}(1 - f_2)I_1(M\rho), \quad (A.27b)$$

where $\rho = r/R$ is the normalized spatial coordinate, while $G_{(ij)}$ and $G_{[ij]}$ denote the ij-component of sym(G) and skw(G), respectively. These equations are now substituted in Eq. (A.4) to obtain the solution of the velocity field.

A.4 Solution for the velocity field

The derived solutions for the micro-motion G_{rz} and G_{zr} are substituted in Eq. (A.4). This yields the velocity gradient:

$$v'(r) = \frac{1}{\mu + \kappa/2}\left[\frac{rP}{2}\left(1 + \frac{\kappa}{2\mu}\right) - \frac{C_1}{2}I_1(\alpha r)\left(\zeta_1(1 + f_1) + \kappa(1 - f_1)\right)\right.$$
$$\left. - \frac{C_2}{2}I_1(\beta r)\left(\zeta_1(1 + f_2) + \kappa(1 - f_2)\right)\right]. \quad (A.28)$$

This expression can be integrated, which yields the general solution for the velocity field

$$v(r) = \frac{1}{\mu + \kappa/2}\left[\frac{r^2 P}{4\mu}\left(\mu + \frac{\kappa}{2}\right) - \frac{C_1(I_0(\alpha r) - 1)}{2\alpha}\left(\zeta_1(1 + f_1) + \kappa(1 - f_1)\right)\right.$$
$$\left. - \frac{C_2(I_0(\beta r) - 1)}{2\beta}\left(\zeta_1(1 + f_2) + \kappa(1 - f_2)\right)\right] + C_4, \quad (A.29)$$

where C_4 is a constant of integration. Using the homogeneous Dirichlet boundary condition on Γ_1, the constant C_4 is found:

$$C_4 = -\frac{R^2 P}{4\mu} + \frac{1}{\mu + \kappa/2}\left[\frac{C_1(I_0(L) - 1)}{2\alpha}\left(\zeta_1(1 + f_1) + \kappa(1 - f_1)\right)\right.$$

$$+ \frac{C_2(I_0(M) - 1)}{2\beta}\Big(\zeta_1(1 + f_2) + \kappa(1 - f_2)\Big)\Bigg].$$

Finally, C_4 is substituted in Eq. (A.29), and the velocity field for a micromorphic pipe flow reads

$$\frac{v(\rho)}{v_0} = 1 - \rho^2$$
$$+ \frac{1}{\mu + \kappa/2}\Bigg[\frac{C_{1\star}(I_0(L) - I_0(L\rho))}{2L}\Big(\zeta_1(1 + f_1) + \kappa(1 - f_1)\Big)$$
$$+ \frac{C_{2\star}(I_0(M) - I_0(M\rho))}{2M}\Big(\zeta_1(1 + f_2) + \kappa(1 - f_2)\Big)\Bigg].$$
(A.30)

B Investigation of experimental data from Bugliarello and Sevilla [4]

The experimental data from Bugliarello and Sevilla originates from a pressure-driven flow, and therefore, the characteristic diagram linking the pressure gradient to the volume flow rate were published in [4]. With the
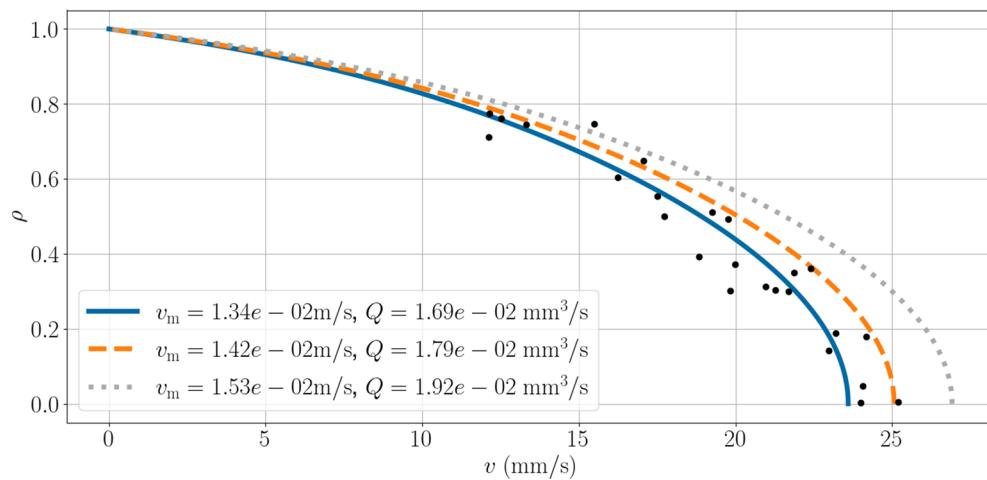

Fig. 17 Comparison of different micromorphic velocity profiles and experimental data from [4] at $R = 20 \times 10^{-6}$m and with $v_m = 1.53 \times 10^{-2}$ms^{-1}
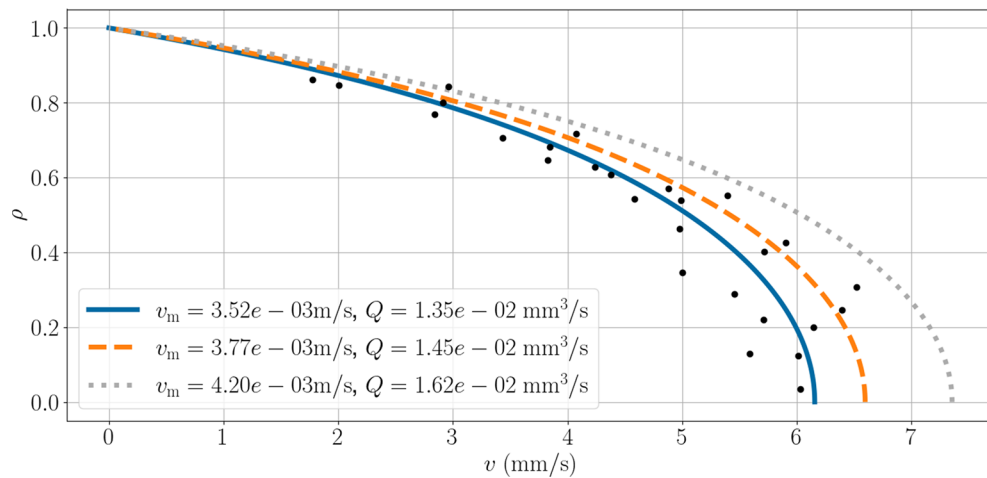

Fig. 18 Comparison of different micromorphic velocity profiles and experimental data from [4] at $R = 35 \times 10^{-6}$m with $v_m = 4.2 \times 10^{-3}$ms^{-1}

help of the volumetric velocity $v_{\mathrm{m}} = Q/(\pi R^2)$, the volume flow rate can be computed, and the corresponding pressure gradient can be extracted from said plots. The knowledge of Q and P enables the computation of v_0 and with it a proper normalization of the velocity profiles. In order to verify that the experimental data matches the volumetric velocity, a micromorphic fluid was fitted to the data and v_{m} was computed for different v_0, see Figs. 17 and 18. For both $R = 20\,\mu\mathrm{m}$ and $R = 35\,\mu\mathrm{m}$, the normalization term v_0 was chosen such that $a)$ v_{m} corresponds to the published value (dotted line), $b)$ the error between velocity profile and data is minimal (solid line), and $c)$ the velocity profile matches the data better and there exists a data point in the characteristic diagram (dashed line). In the end, the reference velocity v_0 was computed using the pressure gradient yielded by the dashed velocity profiles. This corresponds to the data points at $(5.25 \times 10^5 \mathrm{kgm}^{-2}\mathrm{s}^{-2},\ 1.17 \times 10^{-2}\mathrm{mm}^3\mathrm{s}^{-1})$ and $(7 \times 10^4 \mathrm{kgm}^{-2}\mathrm{s}^{-2},\ 1.45 \times 10^{-2}\mathrm{mm}^3\mathrm{s}^{-1})$ for $R = 20\,\mu\mathrm{m}$ and $R = 35\,\mu\mathrm{m}$, respectively. The viscosity coefficient μ in v_0 corresponds to the asymptotic viscosity for large radius taken from [19], because the test conditions of the two studies were alike: Both [19] and [4] investigated the behavior of RBCs suspended in ACD at approximately $25\,^\circ\mathrm{C}$. It should be noted that due to the inconsistency within the experimental data, it cannot be assured that this normalization reflects the actual experimental results accurately. However, since the Fåhræus–Lindqvist effect is satisfactorily reproduced by the micromorphic fluid model, it is also assumed that the micromorphic fluid exhibits a similar volume flow rate as an actual RBC suspension in pressure-driven pipe flows at large shear rates.

References

1. Ariman, T.: On the analysis of blood flow. J. Biomech. **4**(3), 185–192 (1971). https://doi.org/10.1016/0021-9290(71)90003-0
2. Barbee, J.H., Cokelet, G.R.: The fahraeus effect. Microvasc. Res. **3**(1), 6–16 (1971). https://doi.org/10.1016/0026-2862(71)90002-1
3. Baskurt, O.K., Meiselman, H.J.: Blood rheology and hemodynamics. Semin. Thromb. Hemostasis **29**(5), 435–450 (2003). https://doi.org/10.1055/s-2003-44551
4. Bugliarello, G., Sevilla, J.: Velocity distribution and other characteristics of steady and pulsatile blood flow in fine glass tubes. Biorheology **7**(2), 85–107 (1970). https://doi.org/10.3233/bir-1970-7202
5. Chien, S.: Biophysical behavior of red cells in suspensions. In: The Red Blood Cell, pp. 1031–1133. Elsevier (1975). https://doi.org/10.1016/B978-0-12-677202-9.50019-8
6. Eringen, A.: Simple microfluids. Int. J. Eng. Sci. **2**(2), 205–217 (1964). https://doi.org/10.1016/0020-7225(64)90005-9
7. Eringen, A.: Theory of micropolar fluids. Indiana Univ. Math. J. **16**(1), 1–18 (1966). https://doi.org/10.1512/iumj.1967.16.16001
8. Eringen, A., Suhubi, E.S.: Nonlinear theory of simple micro-elastic solids—I. Int. J. Eng. Sci. **2**(2), 189–203 (1964). https://doi.org/10.1016/0020-7225(64)90004-7
9. Eringen, A.C.: Theory of micropolar fluid. J. Math. Mech. **16**(1), 1–18 (1966)
10. Eringen, A.C.: Microcontinuum Field Theories. Springer, New York (1999-)
11. Eringen, A.C.: Microcontinuum Field Theories. Springer, New York (2011)
12. Fåhraeus, R.: The suspension stability of the blood. Physiol. Rev. **9**(2), 241–274 (1929). https://doi.org/10.1152/physrev.1929.9.2.241
13. Fåhræus, R., Lindqvist, T.: The viscosity of the blood in narrow capillary tubes. Am. J. Physiol. Content **96**(3), 562–568 (1931). https://doi.org/10.1152/ajplegacy.1931.96.3.562
14. Goddard, J.D., Miller, C.: Nonlinear effects in the rheology of dilute suspensions. J. Fluid Mech. **28**(4), 657–673 (1967). https://doi.org/10.1017/S0022112067002381
15. Goldsmith, H., Marlow, J.: Flow behavior of erythrocytes. II. Particle motions in concentrated suspensions of ghost cells. J. Colloid Interface Sci. **71**(2), 383–407 (1979). https://doi.org/10.1016/0021-9797(79)90248-0
16. Goldsmith, H.L.: Red cell motions and wall interactions in tube flow. Fed. Proc. **30**(5), 1578–1590 (1971)
17. Goldstein, H., Poole, C.P., Safko, J.L.: Classical Mechanics: Pearson New International Edition, 3rd edn. Pearson, Harlow (2014). https://ebookcentral.proquest.com/lib/kxp/detail.action?docID=5833307
18. Happel, J., Brenner, H.: The viscosity of particulate systems. In: Mechanics of Fluids and Transport Processes, pp. 431–473. Springer Netherlands (1983). https://doi.org/10.1007/978-94-009-8352-6_9
19. Haynes, R.H.: Physical basis of the dependence of blood viscosity on tube radius. Am. J. Physiol. Content **198**(6), 1193–1200 (1960). https://doi.org/10.1152/ajplegacy.1960.198.6.1193
20. Haynes, R.H.: The rheology of blood. Trans. Soc. Rheol. **5**(1), 85–101 (1961). https://doi.org/10.1122/1.548888
21. Haynes, R.H., Burton, A.C.: Role of the non-newtonian behavior of blood in hemodynamics. Am. J. Physiol. Content **197**(5), 943–950 (1959). https://doi.org/10.1152/ajplegacy.1959.197.5.943
22. Kang, C., Eringen, A.: The effect of microstructure on the rheological properties of blood. Bull. Math. Biol. **38**(2), 135–159 (1976). https://doi.org/10.1016/S0092-8240(76)80030-4
23. Késmárky, G., Kenyeres, P., Rábai, M., Tóth, K.: Plasma viscosity: a forgotten variable. Clin. Hemorheol. Microcirc. **39**(1–4), 243–246 (2008)
24. Lanotte, L., Mauer, J., Mendez, S., Fedosov, D.A., Fromental, J.M., Claveria, V., Nicoud, F., Gompper, G., Abkarian, M.: Red cells' dynamic morphologies govern blood shear thinning under microcirculatory flow conditions. Proc. Natl. Acad. Sci. USA **113**(47), 13289–13294 (2016). https://doi.org/10.1073/pnas.1608074113

25. Poiseuille, J.: Recherches experimentales sur le mouvement des liquides dans les tubes de tres-petits diametres. Université La Sapienza de Rome (Biblioteca di Ingegneria Civile, Edile e Ambientale) (1844). https://books.google.de/books?id=uBN1Q-IRzTMC

26. Pop, G.A.M., Duncker, D.J., Gardien, M., Vranckx, P., Versluis, S., Hasan, D., Slager, C.J.: The clinical significance of whole blood viscosity in (cardio)vascular medicine. Neth. Heart J. **10**(12), 512–516 (2002)

27. Pries, A.R., Neuhaus, D., Gaehtgens, P.: Blood viscosity in tube flow: dependence on diameter and hematocrit. Am. J. Physiol. Heart Circ. **263**(6), H1770–H1778 (1992). https://doi.org/10.1152/ajpheart.1992.263.6.h1770

28. Rana, A., Westein, E., Niego, B., Hagemeyer, C.E.: Shear-dependent platelet aggregation: mechanisms and therapeutic opportunities. Front. Cardiovasc. Med. **6**, 141 (2019). https://doi.org/10.3389/fcvm.2019.00141

29. Reinke, W., Johnson, P.C., Gaehtgens, P.: Effect of shear rate variation on apparent viscosity of human blood in tubes of 29 to 94 microns diameter. Circ. Res. **59**(2), 124–132 (1986). https://doi.org/10.1161/01.res.59.2.124

30. Robertson, A.M.: Review of relevant continuum mechanics. In: Hemodynamical Flows, Oberwolfach Seminars, vol. 37, pp. 1–62. Birkhäuser Basel, Basel (2008). https://doi.org/10.1007/978-3-7643-7806-6_1

31. Schofield, R.K., Blair, G.W.S.: The influence of the proximity of a solid wall on the consistency of viscous and plastic materials. IV. J. Phys. Chem. **39**(7), 973–982 (1935). https://doi.org/10.1021/j150367a008

32. Secomb, T.: Mechanics of blood flow in the microcirculation. Symp. Soc. Exp. Biol. **49**, 305–321 (1995)

33. Secomb, T.W.: Blood flow in the microcirculation. Annu. Rev. Fluid Mech. **49**(1), 443–461 (2017). https://doi.org/10.1146/annurev-fluid-010816-060302

34. Silber, G., Trostel, R., Alizadeh, M., Benderoth, G.: A continuum mechanical gradient theory with applications to fluid mechanics. J. Phys. IV **08**(PR8), Pr8-365–Pr8-373 (1998). https://doi.org/10.1051/jp4:1998845

35. Simha, R.: A treatment of the viscosity of concentrated suspensions. J. Appl. Phys. **23**(9), 1020–1024 (1952). https://doi.org/10.1063/1.1702338

36. Vilchevskaya, E.N., Müller, W.H., Eremeyev, V.A.: Extended micropolar approach within the framework of 3m theories and variations thereof. Continuum Mech. Thermodyn. **34**(2), 533–554 (2022). https://doi.org/10.1007/s00161-021-01072-6

37. Wells, R., Schmid-Schönbein, H.: Red cell deformation and fluidity of concentrated cell suspensions. J. Appl. Physiol. **27**(2), 213–217 (1969). https://doi.org/10.1152/jappl.1969.27.2.213

38. (WHO), W.H.O.: The top 10 causes of death (2021). https://www.who.int/news-room/fact-sheets/detail/cardiovascular-diseases-(cvds)